H_2 and CH_4 outgassing rates in the Samail ophiolite, Oman: Implications for low-temperature, continental serpentinization rates

James Andrew Leong[1#], Michael Nielsen[1], Noah McQueen[2], Rūta Karolytė[3], Darren J. Hillegonds[3], Chris Ballentine[3], Tom Darrah[4], Wade McGillis[1,5], and Peter Kelemen[1]

[1]Lamont-Doherty Earth Observatory, Columbia University, NY, USA

[2]School of Engineering and Applied Science, University of Pennsylvania, PA, USA

[3]Department of Earth Sciences, University of Oxford, UK

[4]School of Earth Sciences, The Ohio State University, OH, USA

[5]College of Engineering, University of Notre Dame, IN, USA

[#]corresponding author: jleong@ldeo.columbia.edu

Abstract

Reduced (H_2- and CH_4-rich) and hyperalkaline fluids are products of subsurface reactions accompanying serpentinization of ultramafic rocks. H_2 and CH_4 produced during serpentinization can fuel microorganisms and support habitable subsurface environments. CH_4 is also a potent greenhouse gas and can offset negative greenhouse emissions arising from active CO_2 removal accompanying carbon mineralization in ultramafic rocks. However, the rate at which reduced volatiles are delivered to the surface and the rate of reactions that generate these volatiles at low-temperature conditions are poorly known. In this work, we measured H_2 and CH_4 outgassing rates in several hyperalkaline spring sites in the Samail ophiolite, Oman. H_2 and CH_4 outgassing in these sites are variable and range up to 70,000 and 7,000 moles yr^{-1}, respectively. CH_4 outgassing in spring sites are unlikely to offset negative carbon emissions estimated from active carbon mineralization reactions in the Samail ophiolite. However, diffused

CH_4 outgassing from peridotite outcrops remain unconstrained. Compositional and isotopic constraints show that volatiles are likely derived from active serpentinization, fluid inclusion decrepitation, or a combination of both. Calculated active serpentinization rates of up to 8×10^{-14} sec^{-1} account for measured outgassing rates and these are consistent with slow rates expected at low temperatures. In calculations of serpentinization rates, this work uses reaction-path models to account incorporation of both ferrous and ferric iron in the resulting alteration assemblages, which yields ~0.3 moles H_2 kg^{-1} of ultramafic rock altered, lower than simulations based on iron oxidation to magnetite only. Contribution from decrepitation of H_2- and CH_4-bearing fluid inclusions is possible but would require much more mass of ultramafic rocks to account for observed outgassing. Further studies can help quantify extents of each source on active outgassing in Oman. Overall, this work shows that low-temperature serpentinization on geologically short timescales can account for observed flux of reduced volatiles in hyperalkaline environments.

Keywords

serpentinization; hydrogen (H_2); methane (CH_4); greenhouse emissions; gas flux

1. Introduction

Hyperalkaline (pH >11) and reduced (H_2- and CH_4-rich) fluids in uplifted orogenic and ophiolitic bodies are products of subsurface reactions accompanying the serpentinization of ultramafic rocks such as peridotites. In the process of serpentinization, the original minerals that comprise peridotites such as olivine and pyroxene are mostly replaced by hydrous serpentine minerals upon interaction with water. In turn, reacting fluids become highly reduced and alkaline. Reflecting these reducing conditions, peridotite-hosted, alkaline springs are often characterized by continuous bubbles composed of H_2- and CH_4-rich gas. At springs and in boreholes, the temperature of hyperalkaline fluids hosted in ultramafic bodies in continents rarely exceeds 50 °C (Leong & Shock, 2020; Suda et al., 2014). These low-temperature, H_2- and CH_4-rich fluids fuel chemotrophic microbial communities and have profound implications for the habitability of Earth's ultramafic aquifers (Schrenk et al., 2013; Templeton et al., 2021) as well as in ice-covered ocean worlds in the outer Solar System where ultramafic minerals are believed to be present in contact with water (Glein and Zolotov, 2020).

Subsurface carbon mineralization reactions, in particular formation of Mg-carbonate (e.g., magnesite and dolomite) veins, accompany subsurface serpentinization of Mg-rich ultramafic rocks (Mervine et al., 2014). Furthermore, Ca-rich and alkaline fluids that discharge back to the surface further react with atmospheric CO_2 to form Ca-carbonates (e.g., calcite) (Mervine et al., 2014; Falk et al., 2016). These systems could potentially be accelerated to curb increasing levels of atmospheric CO_2 (Goff & Lackner, 1998; Kelemen et al., 2011, 2020; Kelemen & Matter, 2008; Matter & Kelemen, 2009; National Academies of Sciences, Engineering, and Medicine, 2019; Wilson et al., 2010). For example, the Samail ophiolite, which hosts the world's largest subaerial exposure of ultramafic rocks, is estimated to sequester 10,000 to 100,000 metric tons of CO_2 annually through active carbon mineralization and serpentinization (Kelemen & Matter, 2008). However, water-rock interactions can also generate significant amounts of CH_4, a potent greenhouse gas. Thus, quantifying the rates of outgassing of reduced volatiles in ophiolites can help inform consequences of future CO_2 sequestration and storage strategies targeting ultramafic aquifers on Earth.

Since the initial reports of Barnes et al. (1967), low-temperature serpentinization-generated fluids hosted in continents have been documented in more than 20 localities across the planet (see Etiope et al., 2017; Leong & Shock, 2020). While the compositions of these fluids are now well known, the rate at which hyperalkaline fluids and reduced volatiles are generated during low-temperature serpentinization is poorly known. Experiments reporting considerable H_2 and/or CH_4 production via low-temperature serpentinization (Neubeck et al., 2011, 2014; Mayhew et al., 2013; Okland et al., 2014) have been recently questioned (McCollom and Donaldson, 2016). McCollom & Donaldson (2016) showed that H_2 production rates in experimental runs simulating low-temperature serpentinization are very slow and indistinguishable from blank experiments. Additional constraints on the rate of low-temperature serpentinization can be provided by natural observations. Recent ^{14}C analysis of CH_4 dissolved in water samples from hyperalkaline wells in the Samail ophiolite in Oman showed that their sources are young, suggesting active generation of reduced volatiles (Nothaft, 2020). Kelemen et al. (2021) found measurable ^{14}C in 23 of 35 samples of carbonate veins in serpentinized peridotite drill core from Oman, intergrown with, and cut by, serpentine veins, yielding an order of magnitude rate estimate of 1 vol% per 10,000 years. Paukert Vankeuren et al. (2019) showed that hyperalkaline groundwater sampled from the Samail ophiolite could have been recharged during the last glacial age (~10,000 – 20,000 years ago). These observations based on natural samples show that low-temperature serpentinization can actively yield hyperalkaline fluids and reduced volatiles on geologically short timescales. As often the case in metamorphic geology, field-based observations can supplement and provide further constraints on processes often requiring lengths of time not possible in a laboratory experiment.

The rates at which reduced volatiles such as H_2 and CH_4 are outgassed in serpentinization-generated alkaline springs can inform us on the rate of serpentinization reactions that generated these volatiles. H_2 is generated via the oxidation of ferrous iron in reacting phases to ferric iron in secondary minerals, e.g., magnetite, coupled to the reduction of H_2O to H_2, as depicted by the simplified reaction,

$$3\mathrm{Fe(II)O}_{(\mathrm{Fe(II)\text{-}bearing\ minerals})} + \mathrm{H_2O} \rightarrow \mathrm{Fe(II)Fe(III)_2O}_{4(\mathrm{magnetite})} + \mathrm{H_2}. \text{ (Reaction 1)}$$

Reaction (1) shows that a mole of H_2 is generated from the oxidation of two moles of Fe mobilized from primary minerals (e.g., Fe(II)-bearing olivine and pyroxene) or pre-existing Fe(II)-bearing serpentine and brucite. Ferric iron in secondary phases is often attributed to magnetite but studies have shown that ferric iron can be also hosted in serpentine (Andreani et al., 2013; Ellison et al., 2021; Klein et al., 2009, 2014; Mayhew et al., 2018; Mayhew & Ellison, 2020; O'Hanley & Dyar, 1993, 1998; Streit et al., 2012), especially at low-temperature conditions (Klein et al., 2014). A kilogram of peridotite typically contains 100 grams of FeO (10 wt%) or 1.4 moles FeO and thus, has the potential to generate 0.47 moles H_2 if reaction (1) proceeds to completion. Serpentine minerals can host both ferrous and ferric iron with a Fe(III)/ΣFe ratio less than that of magnetite, *i.e.*, 0.67 (Andreani et al., 2013; Mayhew et al., 2018; Mayhew & Ellison, 2020). Thus, reaction (1) above represents an upper bound on the H_2-generation potential of a given amount of peridotite. In ophiolitic serpentinites, the average Fe(III)/ΣFe ratio is 0.45 (Mayhew and Ellison, 2020). Thus, serpentinization of a kg of peridotite is likely to generate less than 0.47 moles of H_2.

As fluids become more H_2-rich, the reduction of oxic carbon species (e.g., CO_2) to CH_4 via

$$\mathrm{CO_2} + 4\mathrm{H_2} \rightarrow \mathrm{CH_4} + 2\mathrm{H_2O} \text{ (Reaction 2)}$$

becomes favorable. Reaction (2) can proceed abiotically (Berndt et al., 1996; Horita and Berndt, 1999; McCollom and Seewald, 2003, 2007; Seewald et al., 2006; McCollom, 2016) or facilitated by microorganisms (i.e., methanogens, Schrenk et al., 2013). In reaction (2), formation of a mole of CH_4 consumes four moles of H_2 generated via rock alteration. Methane generation, either abiotic or microbial, may require less H_2 if the reactant carbon species such as carbon monoxide, formate, and acetate (Kohl et al., 2016; Crespo-Medina et al., 2017) is less oxidized as CO_2.

Despite these complicating factors, in theory the rate of reduced gas (H_2, CH_4) formation can be related to the rate of rock alteration, i.e., serpentinization. In turn, at steady state, the observed rate of reduced gas outgassing is less than or equal to the rate at which it forms. Overall, quantifying the rate of H_2 and CH_4 outgassing can potentially constrain the rate to which reaction (1) proceeds.

While alkaline continental seeps and submarine vents are evidence of active serpentinization, recent studies have argued that H_2 and particularly CH_4 outgassed from low-temperature serpentinizing environments do not result from ongoing alteration reactions in subsurface aquifers (McDermott et al., 2015; Wang et al., 2018). Instead, pre-existing H_2 and CH_4 are said to be liberated during ongoing low-temperature submarine hydrothermal circulation from ancient fluid inclusions that host gases formed when the system was hotter in the past (Klein et al., 2019; Grozeva et al., 2020). Thus, observed H_2 and CH_4 outgassing rates may represent "decrepitation" rates instead of present-day serpentinization rates. In practice, it is likely that H_2 and CH_4 outgassing in low-temperature serpentinizing environments results from a combination of active serpentinization and fluid inclusion decrepitation, with the proportions varying from place to place.

In this work, we measured H_2 and CH_4 outgassing rates in several hyperalkaline spring sites in the Samail ophiolite. From field-determined outgassing rates, we constrained possible rates of active serpentinization and decrepitation, assuming outgassing is a result of either of the above processes. Additional input from fluid inclusion decrepitation would be warranted if calculated outgassing-derived rates exceed rates informed by temperature-rate fits derived from laboratory-based serpentinization experiments. In calculations of active alteration or serpentinization rates, this work uses reaction-path models to account for incorporation of both ferrous and ferric iron in the resulting alteration assemblages to better reflect constraints from analysis of ferrous-to-ferric iron ratios in serpentinization products.

2. Methods

2.1 Field and Laboratory Methods

Outgassing rates and gas samples were taken from six hyperalkaline spring sites in the Samail ophiolite: Haylayn, Al Bana, Shumayt, Dima, Al Hilayw, and Misfah. Locations of these sites are shown in Figure 1. These sites host hyperalkaline seeps and pools (Figure 2a) that often co-occur with gas bubbles (Figure 2b), except for Al Hilayw where bubbling was not observed. The majority of these sites have several bubbling point sources (>30). Springs in Dima are less active with only 3 to 5 identified bubbling point sources. The pH and temperature of hyperalkaline pools where bubbling was observed were measured using temperature sensors and pH electrodes (WTW™ SenTix™ 41 gel electrode) attached to a WTW™ 3300*i* meter. The electrodes were calibrated using 7.0, 10.01, and 12.46 pH buffers in the field. The locations, pH and temperature of hyperalkaline samples sites are documented in Table 1.

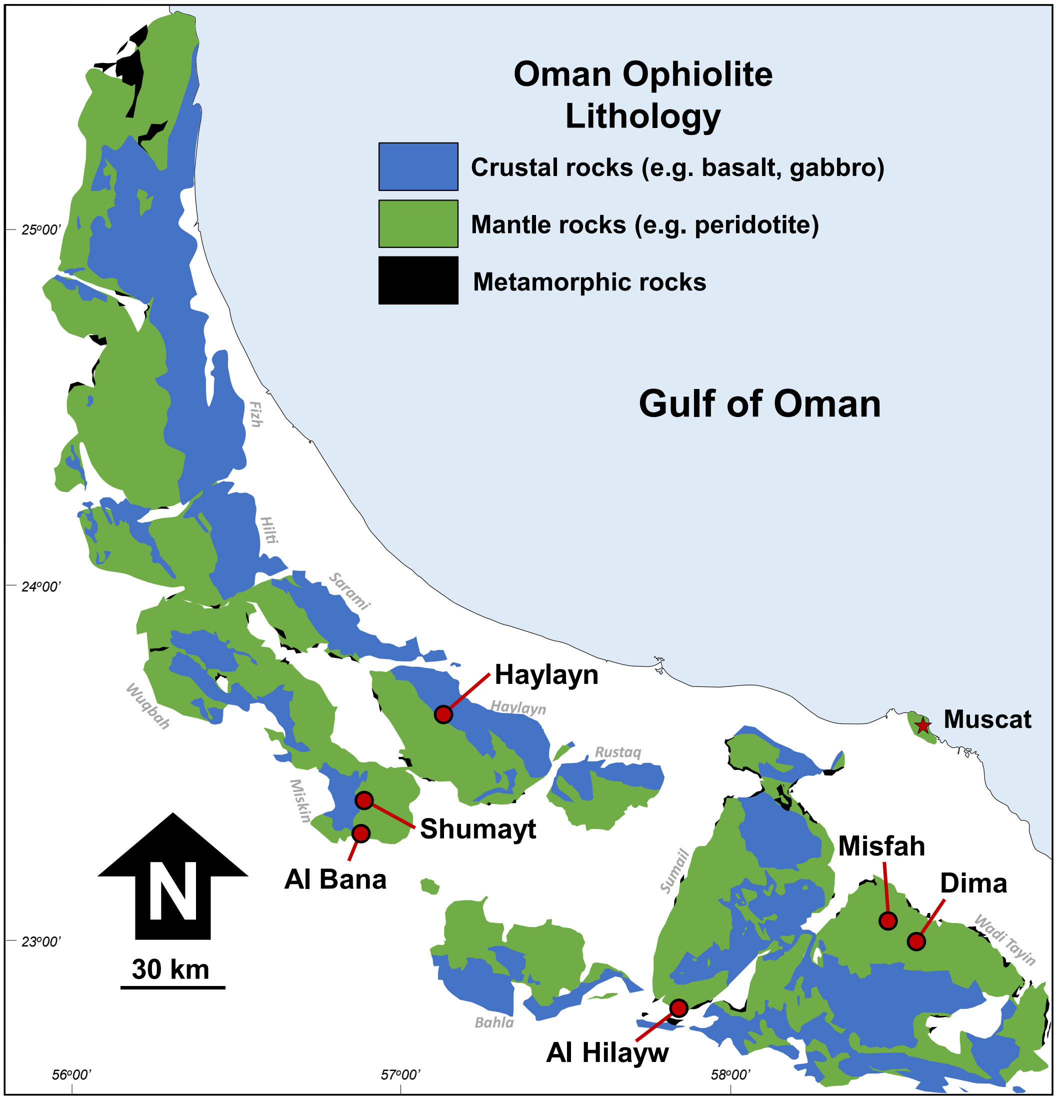

Figure 1. Study sites investigated in this work overlain in a geological map of the Oman ophiolite modified from Nicolas et al. (2000).

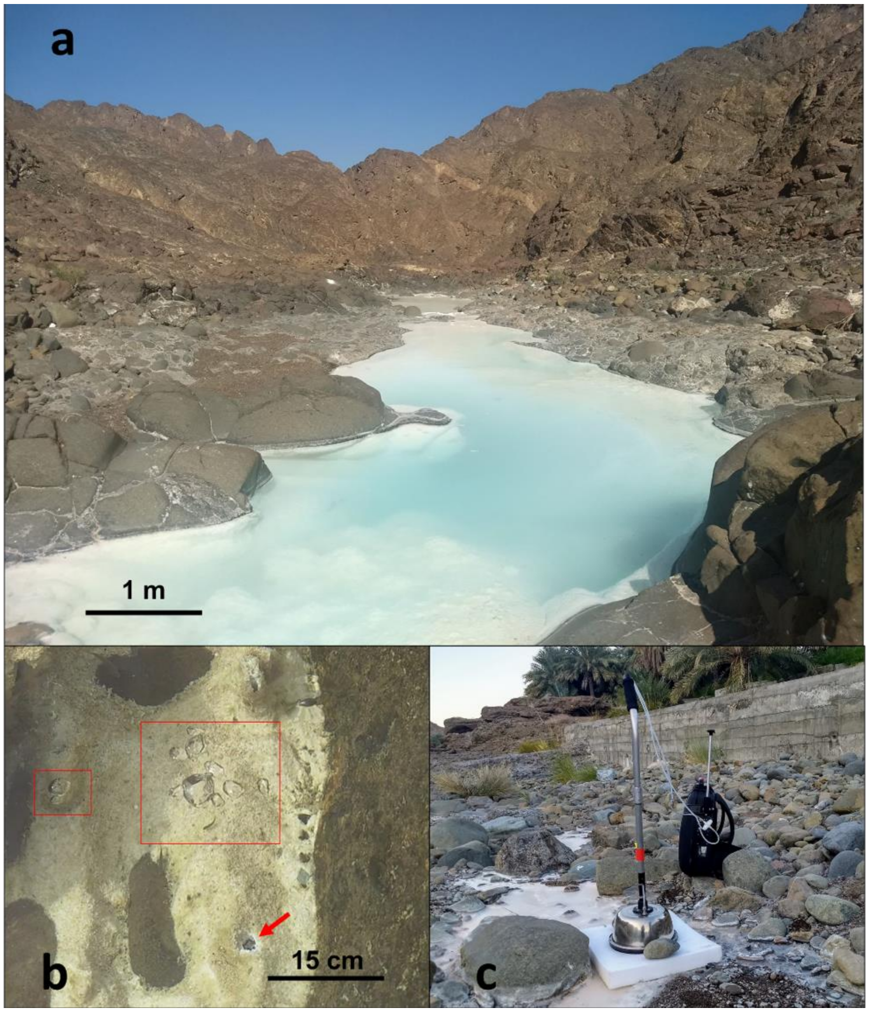

Figure 2. (a) Hyperalkaline stream in Misfah, Oman. (b) Gas bubble seeping out into stream water in Shumayt. (c) Picarro gas detector (black bag) connected to a mobile flux system (steel bowl) over an alkaline seep at Haylayn.

Outgassing rates for CH_4 were determined using the Picarro GasScouter^{TM} G4301 equipped with a GPS kit and mobile soil flux system (Figure 2c). This portable battery-powered analyzer can simultaneously measure temperature, pressure, and CH_4, CO_2, and H_2O concentrations (i.e., humidity) using a cavity ring-down spectrometer. Typical precision and detection limits for CH_4 are 3 (+0.1% of reading) and 0.9 ppb, respectively, over a measurement range of up to 800 ppm. While CO_2 is measured, we only report CH_4 measurements in this work. Flux experiments were conducted using a dome-shaped mobile soil flux system (dome base area: 615 cm^2, dome volume; volume: 9.3 L) above bubbling sources, non-bubbling hyperalkaline pools, surrounding circumneutral steams/pools, and nearby soils. For measurement above hyperalkaline springs and surrounding circumneutral streams, the mobile flux system was placed over bubble sources using a styrofoam flotation device for several minutes (1 to 5 min) or within seconds if the upper measuring range of 800 ppm is attained. Measurement interval is 3 seconds. Outgassing rates in nearby non-hyperalkaline streams as well as soils were also measured using the mobile soil flux system for durations ranging from 1 to 5 minutes. CH_4 flux rates were determined immediately after the experiments using the Picarro Soil Flux Processor lite for a smart phone or tablet connected to the detector using a flux fitter model following Hutchinson & Mosier (1981), accounting for the temperature, pressure, and humidity measured simultaneously with the CH_4 concentration.

Table 1. Temperature, pH, and locations of hyperalkaline spring sites in Oman studied by this work.

Sites	**Location**		**pH**	**T (°C)****
	Lat	**Long**		
Haylayn	23.6277	57.1152	10.79*	28.2
Al Bana	23.2883	56.8978	11.17	37.4
Shumayt	23.4056	56.8629	11.50	34.0
Dima	22.9841	58.5946	11.21	33.0
Misfah	23.0364	58.4931	11.14	36.7
Al Hilayw	22.8145	57.8368	11.54	30.1

*End-member pH was not determined as bubbling seeps are under the stream bed. Indicated pH is the maximum value recorded by the pH meter as close as to the seep source.

**Sampling dates were from February 26, 2020 to March 06, 2020. Historical February - March average maximum temperatures from the Rustaq (near Haylayn), Ibri (near Al Bana and Shumayt), Nizwa (near Al Hilayw), and Ibra (near Misfah and Dima) weather stations are 27 – 32 °C, 28 – 32 °C, 30 – 32 °C, 26 – 30 °C, respectively. Non-alkaline surface pools and streams, which has equilibrated with the atmosphere, at Shumayt and Misfah during day of sampling is 26.4 °C and 23 - 29.5 °C, respectively.

Outgassing rates for H_2 were measured using a Honeywell ToxiRae Pro gas detector for H_2. The detector measures H_2 via an electrochemical sensor over a range of 0 to 1000 ppm with a resolution of 10 ppm. The detector was calibrated prior to being brought in the field using an air blank and 1000 ppm H_2 standard. As we were only able to do a two-point calibration, we had not determined the accuracy and precision of the H_2 sensor. Previous works determined the accuracy of electrochemical H_2 sensors to be around ~10% of reading (Zgonnik et al., 2019). The detector was placed inside a 50 L sealed chamber in which H_2 outgassed from a bubbling source was collected using an inverted funnel, and allowed to accumulate over time. Experimental durations were up to 10 minutes, or less when the upper measuring range of 1000 ppm was attained, signaled via an audible alarm. Measurement interval is either 5 or 10 seconds. The H_2 detector is not sensitive enough to detect changes in H_2 concentration above non-bubbling pools and soils and thus, was only used on bubbling pools. Since temperature, pressure, and humidity were not simultaneously measured in the experiment, H_2 flux rate was simply calculated from the difference in the starting and ending H_2 concentrations in the accumulation chamber for the given experimental duration.

Gas samples for major gas concentration and noble gas concentration and isotopes were collected using the inverse funnel method. A funnel connected to a copper tube via gas-impermeable plastic tubing was filled with the spring water in bubbling sites. The copper tube was sealed using clamps after gas bubbles from the springs displaced the spring water in the tubes.

Composition of major gases (H_2, N_2, O_2, H_2S, Ar, CH_4, C_2H_6, C_3H_8, and C_4H_{10}) were measured at the Wheel Laboratory at Ohio State University using a combination of an SRS Residual Gas Analyzer 300 AMU Quadrupole Mass Spectrometer (MS) and a ThermoFisher Trace 1310 Gas Chromatograph (GC) equipped with a thermal conductivity detector (TCD) and flame ionization detector (FID). Samples stored in the copper tubes were liberated on a vacuum line and fed through multiple detectors in the gas chromatograph. More details on methods and analytical precision can be found in Darrah et al. (2015) and Moore et al. (2020).

Analyses of noble gas concentrations and isotopes (He, Ne, Ar, Kr, Xe) were conducted at the Noble Gas Laboratory at the University of Oxford following methods detailed in Barry et al. (2016) and Byrne et al. (2018). In summary, gas stored in copper tubes was mobilized into a vacuum line connected to a series of purification and reactive gas removal chambers. A Hiden Analytical HAL-201 quadrupole mass spectrometer was used for preliminary noble gas quantitation and to ensure adequate purification. Helium (He) was first measured using the ThermoScientific Helix SFT multicollector mass spectrometer while the rest of the noble gases (Ne, Ar, Kr, Xe) were measured using the ThermoScientific Argus VI multicollector mass spectrometer. All 23 stable noble gas isotopes were measured during the total run.

2.2 Thermodynamic Simulations

The amount of H_2 that can be potentially generated via the serpentinization or alteration of a given mass or volume of peridotite was estimated using mass-transfer calculations. These calculations were conducted using the speciation and reaction-path code, EQ36 (Wolery and Jarek, 2003). Model setup is similar to that of Leong & Shock (2020). Reactants were global average rainwater (Berner and Berner, 2012) and Samail ophiolite harzburgite with an average composition taken from Hanghøj et al. (2010). Calculations were conducted under ambient conditions (25 °C, 1 bar) to simulate near surface reactions and an open-system flowthrough pathway which tracks the compositions of coexisting solids and fluids as the rock alteration process proceeds. The progress of rock alteration reactions simulates subsurface flow where fluids encounter and react with more and more rock. The amount of H_2 generated, per amount of rock that was altered, was tracked in terms of moles H_2 and CH_4 generated per m^3 rock. The rate to which rocks are actively altered (m^3 rock per year) is then estimated by relating these values with measured volatile outgassing rates from field experiments (mole H_2 or CH_4 outgassed per year), assuming all volatiles generated during alteration are outgassed into the surface at steady state.

3. Results

3.1 Gas compositions of Oman hyperalkaline seeps

Compositions of gases sampled from the study sites are presented in Table 2 and illustrated in Figure 3a. Gases sampled from Haylayn and Shumayt are predominantly composed of H_2. Unfortunately, gas sampled from Al Bana was contaminated by ambient air during sampling or had leaked during storage. However, prior work has shown that gas from this site is also mostly H_2 (Canovas et al., 2017; Howells et al., 2022). Outgassing in Misfah is mostly composed of H_2 with some N_2. Overall, as shown in Figure 2a, compositions of gases sampled from the above spring sites are consistent with findings from prior work conducted in Oman where most of gases are predominantly composed of H_2 and with a minor to significant N_2 component (Boulart et al., 2013; Canovas et al., 2017; Howells et al., 2022; Neal & Stanger, 1983; Sano et al., 1993; Vacquand et al., 2018; Zgonnik et al., 2019).

Table 2. Composition of major gas collected from each sample sites.

Sites	**H_2**	**CH_4**	**N_2**	**O_2**	**CO_2**	**Ar**	**H_2S**	**C_2H_6**	**C_3H_8**	**i-C_4H_{10}**	**n-C_4H_{10}**	**H_2/CH_4**	**$CH_4/C_2 + C_3$**
	vol %	vol %	vol %	vol %	vol %	vol %	vol %	ppm	ppm	ppm	ppm		
Haylayn	86.4	6.7	6.8	bdl	0.1	0.0	bdl	29.1	10.3	bdl	bdl	12.9	1702
	87.1	6.9	5.9	bdl	0.1	0.0	bdl	32.3	14.0	bdl	bdl	12.6	1488
Al Bana	*bdl*	*0.01*	*78.5*	*21.4*	*0.1*	*0.9*	*bdl*	*bdl*	*bdl*	*bdl*	*bdl*	*n/a*	*n/a*
Shumayt	93.8	2.2	4.0	bdl	0.1	0.1	bdl	6.9	1.7	bdl	bdl	42.7	2568
Dima	7.8	50.5	41.4	bdl	0.2	0.4	bdl	243.0	123.7	88.8	51.9	0.2	1377
Misfah	66.9	7.2	25.7	bdl	0.2	0.1	bdl	85.2	12.6	10.2	5.0	9.3	736

Notes: Two gas samples were collected at Haylayn. The Al Bana sample was contaminated by ambient air and hence is italicized. "bdl" means below detection limit.

In contrast, gas from Dima is composed mostly of CH_4 and N_2, which has not been previously observed in Oman. The closest analogues for these CH_4- and N_2-rich samples are those sampled from hyperalkaline seeps in the Voltri massif in Italy (Boulart et al., 2013) and Kizildag in Turkey (D'Alessandro et al., 2018). So far, no CH_4-dominated gas such as is found in Chimaera (Turkey, Etiope et al., 2011) and Elba (Italy, Sciarra et al., 2019) has been sampled in

Oman. No gas bubbles were observed at pools in Al Hilayw, and thus no gas was sampled there.

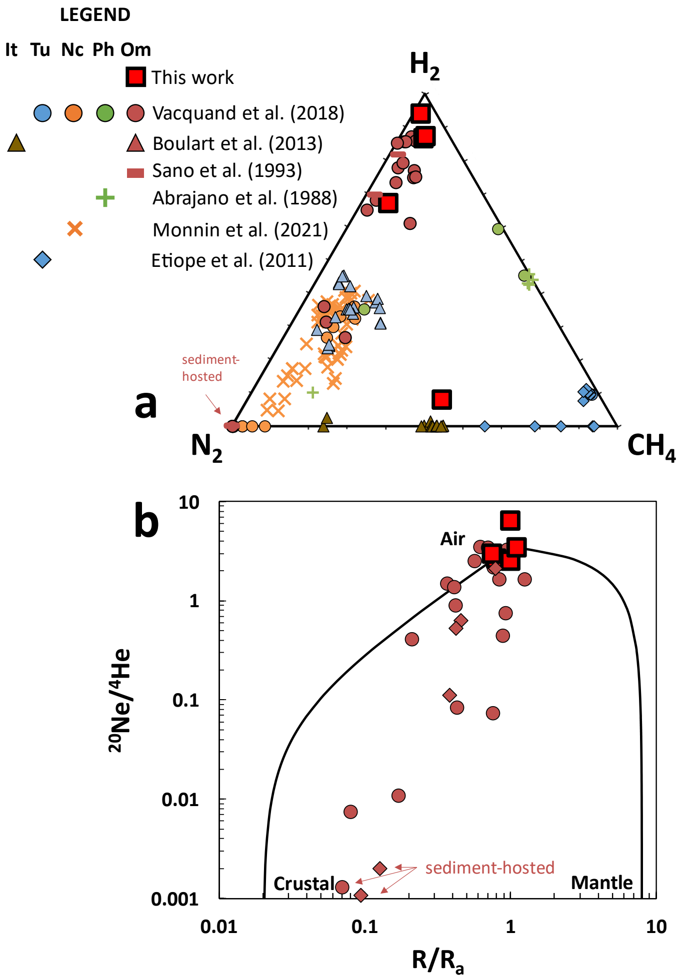

Figure 3. (a) Major gas composition of study samples as well as previous samples taken from Oman and other hyperalkaline sites. (b) Noble gas isotopic trends (R/R_a vs $^{20}Ne/^{4}He$) of study samples relative to existing samples from previous works (Abrajano et al., 1988; Boulart et al., 2013; Etiope et al., 2011; Monnin et al., 2021; Sano et al., 1993; Vacquand et al., 2018) in Italy (It), Turkey (Tu), New Caledonia (Nc), Philippines (Ph), and Oman (Om).

Noble gas isotopic compositions are presented in Table 3 and illustrated in Figure 3b. Full data can be found in Table S1. While all samples plot close that of an air end-member, samples from Haylayn, Al Bana, and Misfah are distinctly different from air at >5σ. The samples from Misfah and Al Bana have the highest (1.11) and lowest (0.75) He isotope ratios, respectively, expressed as observed $^{3}He/^{4}He$ divided by the $^{3}He/^{4}He$ ratio in air, R/R_a. Contribution from ^{3}H (tritium) on a slightly higher $^{3}He/^{4}He$ for the Misfah sample is unlikely as deeply-sourced hyperalkaline fluids in Oman are depleted in this isotope (Paukert Vankeuren et al., 2019). Overall, contributions from mantle and radiogenic sources are minor, with R/R_a values very close to 1 and $^{20}Ne/^{4}He$ ratios ranging from 2 to 7 (Figure 3b). The $^{40}Ar/^{36}Ar$ ratios of study samples (~300, Table 3) also indicate strong atmospheric signatures. These data indicate that outgassing in hyperalkaline seeps in Oman mostly contains noble gases derived from ambient air, consistent with the idea that most of the outgassing H_2 and CH_4 is formed via reaction of ambient groundwater with peridotite.

Table 3. Noble gas compositions (ppmv) and isotope ratios. R/Ra is the helium isotopic ratio normalized to modern air ($R_a = ^{3}He/^{4}He = 1.4x10^{-6}$)

Site	**^{4}He**		**^{20}Ne**		**^{40}Ar**		**^{84}Kr**		**^{132}Xe**	
Haylayn	0.56	*0.006*	1.35	*0.009*	1055	*11*	0.09	*0.001*	0	*3.E-05*
Al Bana	0.7	*0.007*	1.85	*0.012*	1616	*16*	0.14	*0.001*	0.01	*5.E-05*
Shumayt	0.39	*0.004*	1.5	*0.010*	2857	*29*	0.3	*0.002*	0.01	*1.E-04*
Dima	1.75	*0.018*	5.59	*0.036*	4137	*41*	0.3	*0.002*	0.01	*9.E-05*
Misfah	1.62	*0.016*	5.38	*0.035*	5485	*55*	0.46	*0.003*	0.02	*2.E-04*
Air*	5.24		16.45		9303		1.14		0.09	

Note: Full data can be found in Table S1. Values in italics are absolute errors.
*All air noble gas data are from Ojima & Podosek (2002), except for those for Ar which are from Lee et al. (2006).

Table 3. (cont'd)

Site	**R/R_a**		**^{20}Ne/^{4}He**		**^{20}Ne/^{36}Ar**		**^{40}Ar/^{36}Ar**		**^{84}Kr/^{36}Ar**	
Haylayn	0.8	*0.015*	2.4	*0.040*	0.38	*0.008*	298	*1.2*	0.03	*0.001*
Al Bana	0.75	*0.014*	2.65	*0.044*	0.34	*0.007*	296	*1.2*	0.03	*0.001*
Shumayt	1	*0.019*	3.89	*0.064*	0.16	*0.003*	299	*1.2*	0.03	*0.001*
Dima	1	*0.019*	3.19	*0.053*	0.4	*0.008*	299	*1.2*	0.02	*0.000*
Misfah	1.11	*0.021*	3.32	*0.055*	0.29	*0.006*	299	*1.2*	0.03	*0.001*
Air*	1		3.14		0.528		298.6		0.037	

The data also indicate that our gas samples were not significantly contaminated by surrounding air during sampling, as noble gas, N_2 and O_2 concentrations are much lower in sampled gas relative to air (see Tables 2 and 3), except for the contaminated sample from Al Bana for major gas analysis that contains atmospheric gas concentrations. The noble gas compositions in our samples are consistent with most of Oman gas samples previously studied by Vacquand et al. (2018) and Sano et al. (1993). Sites characterized by lower R/R_a and $^{20}Ne/^{4}He$ values, trending towards crustal noble gas components were found in previous studies (Sano et al., 1993; Vacquand et al., 2018), especially at springs in and near outcrops of sedimentary rocks. These sites were not sampled in this work.

3.2 Outgassing rates from bubbling sites

Outgassing rates measured from various field flux experiments are summarized in Table 4 and illustrated in Figure 4. Values shown in Table 4 depict upper bounds on outgassing rates, derived from the maximum measured outgassing rate from individual bubble sources and the maximum estimated number of bubble source for each site, as shown in Supplementary Table S2. Only outgassing rates from bubbling sources were measured using the H_2 detector. Both bubbling and diffuse outgassing were measured using the CH_4 analyzer (see below).

Outgassing rates are calculated from measured changes in the concentration of H_2 and CH_4 that accumulated in a flux chamber of a known volume within a given experimental duration. H_2 values were only reported for bubbling springs and thus all diffuse H_2 values reported in Table 4 were derived from the diffuse CH_4 values and measured H_2/CH_4 ratios shown in Table 2. As shown in Tables 2 and S2, the H_2/CH_4 ratio measured from gas samples taken in Haylayn and Misfah (Table 2) are within range of those measured from the field (Table S2). The gas sample from Dima has a H_2/CH_4 ratio that is slightly lower than those measured via flux experiments in the field, but measurements consistently show that outgassing in Dima has the lowest H_2/CH_4 values amongst all study sites.

Outgassing rates estimated from measured fluxes at bubbling sites in the five study areas are variable. The highest H_2 and CH_4 rates from bubbling sources were measured at Haylayn (up to 71,000 moles H_2 yr^{-1}, 6,700 moles CH_4 yr^{-1}) followed by Al Bana (up to 21,000 moles H_2 yr^{-1}, 1,100 moles CH_4 yr^{-1}), and Misfah (up to 3,600 moles H_2 yr^{-1}, 410 moles CH_4 yr^{-1}). Outgassing from bubbling seeps in Shumayt and Dima was relatively slow (at most 1,000 moles H_2 yr^{-1}, 25 moles CH_4 yr^{-1}). Fluids at Al Bana and Misfah were warmer (37 and 36 °C, respectively, see Table 1) than those at Shumayt and Dima and most other peridotite-hosted alkaline springs in Oman where temperature is typically around 30 °C or less depending on the time of the day it was sampled (Chavagnac et al., 2013; Leong et al., 2021; Paukert et al., 2012). While bubbling in all other sites occurs in predominantly end-member hyperalkaline pools or seeps, gas seepage in Haylayn occurs in a streambed of a circumneutral flowing river. Hence, the pH and temperature for Haylayn in Table 1 pertains to values obtained closest to the bubbling source. End-member fluids there could have higher pH and temperature.

Overall, the highest outgassing rates were measured in the warmer springs, suggesting derivation of more gas from deeper sources. Historical average maximum temperature (February – March) recorded by the Oman Directorate General of Meteorology from weather stations near study sites ranges from 26 to 32 °C (see Table 1 notes). This is consistent with temperatures measured by this work in nearby surficial, non-alkaline pools and streams, which ranges from 23 – 30 °C in Misfah and 26.4 °C in Shumayt. Assuming temperature differences between deep-seated alkaline seeps and the surface of ~6 – 10 °C (36 °C minus 30 or 26 °C) and a typical continental geothermal gradient of ~20 °C per km (Blackwell, 1971), it is likely that a source depth greater than 300 m feeds the alkaline springs.

Table 4. Maximum total outgassing of CH_4 and H_2 (mole yr^{-1}) from bubbling and diffuse sources per site.

Sites	CH_4			H_2		
	bubble	**diffuse**	**total**	**bubble**	**diffuse**	**total**
Haylayn	6,700	640	**7,300**	71,000	*8,200*	**79,000**
Al Bana	1,200	820	**2,000**	21,000	*8,200*	**29,000**
Shumayt	*24*	n.m.	**>24**	1,000	n.m.	**>1,000**
Dima	*140*	4,300	**4,500**	22	*670*	**690**
Misfah	400	2,600	**3,100**	3,600	*25,000*	**28,000**
Al Hilayw	n.o.	120	**120**	n.o.	*1,200*	**1,200**

Note 1: Values are derived by multiplying maximum flux rate in each study site with the maximum estimated number of point source (see Table S2) and area (see Table S3) for bubbling and diffuse sites, respectively, as shown in Table S2. Values are rounded to two significant figures. Estimated uncertainty is at least 10% and 0.1% for H_2 and CH_4 measurements, respectively, based on the instrumental uncertainties mentioned in the methods section.

Note 2: Unitalicized values are from field measurements. Values in italics are estimated from measured H_2/CH_4 shown in Table 2. For Al Bana, we used a ratio of 10 from Canovas et al. (2017). No gas has been sampled in Al Hilayw so we used a H_2/CH_4 ratio (~10) of samples measured by Canovas et al. (2017) in a nearby site (Falaij). Values in bold are sum of bubbling and diffuse values. All values are rounded to at most two significant figures following field flux data (see Table S2).

Note 3: Bubbling was not observed (n.o.) in Al Hilayw. We had not measured (n.m.) diffused flux in Shumayt and reported total outgassing can be considered as a minimum value.

Previous outgassing estimates by Zgonnik et al. (2019) for bubbling sites in Haylayn (1.1 L H_2 hr^{-1} for each of ~20 bubbling source, or ~7,900 moles H_2 yr^{-1}) are within the range of our measured values (2,200 to 71,000 moles H_2 yr^{-1}). Low outgassing rates measured in Shumayt and Dima are consistent with analogous bubbling spring sites in Greece (up to 90 moles CH_4 yr^{-1} in one site, Etiope et al., 2013). However, all sites have outgassing rates that are much lower than that measured in the Chimaera seep in Turkey (190 metric tons or ~12 million moles CH_4 yr^{-1}, Etiope et al., 2011).

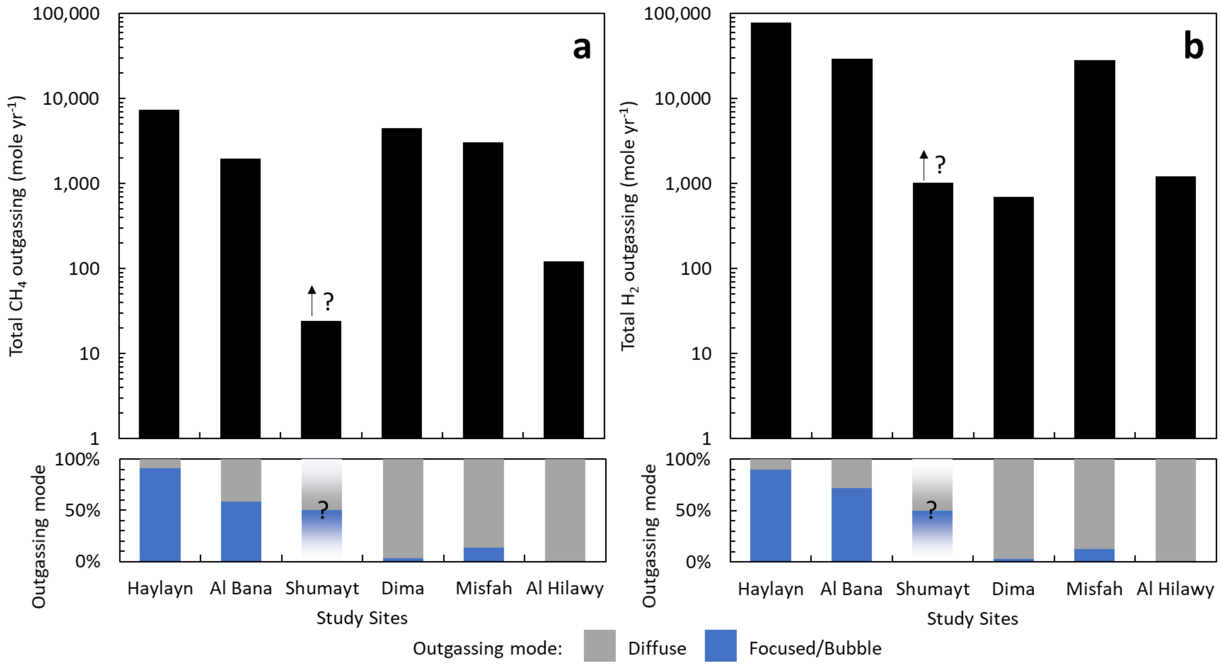

Figure 4. Maximum total CH_4 (a) and H_2 (b) outgassing rates (mole yr^{-1}) measured from each study site. Total outgassing is composed of bubbling (blue) and diffuse (grey) sources as indicated by the bottom charts. Diffuse outgassing was not measured in Shumayt. Hence, the black bar for Shumayt only represents bubbling sources, and total outgassing is unknown, as represented by the arrow and question marks. Outgassing in Haylayn and Al Bana is predominantly from bubbling sources. In contrast, outgassing in Misfah and Al Hilayw is predominantly from diffuse sources.

3.3. Diffuse outgassing rates in hyperalkaline pools

Diffuse CH_4 flux from non-bubbling hyperalkaline pools measured using the Picarro CH_4 analyzer are mostly positive (*i.e.*, outgassing instead of ingassing) as shown in Supplementary Table S3. The standard deviation of field observations is mostly within 10% of flux values. Values reported for diffuse sources in Table 4 were calculated using flux values and the maximum area extent of hyperalkaline pools shown in Supplementary Table S3. No bubbling was observed in Al Hilayw but diffuse CH_4 outgassing was measured, which ranges from 0.1 to 1.2 mole CH_4 m^{-2} yr^{-1}. Assuming hyperalkaline pools in Al Hilayw encompass at most 100 m^2, a total annual outgassing less than or equal to 120 mole CH_4 is derived. In contrast, in some sites such as Dima and Al Bana, diffuse CH_4 outgassing is much higher (e.g., up to 86 mole CH_4 m^{-2} yr^{-1} in Dima). In Dima, hyperalkaline pools comprise at most 50 m^2 in area. Hence, total diffuse outgassing in this site alone (up to 4,300 mole CH_4 yr^{-1}) is comparable to that estimated from outgassing from sites with vigorous bubbling such as Haylayn. Estimates of total outgassing, from both bubbling and diffuse sources, are presented in Table 4 and illustrated in Figure 4. Outgassing in Haylayn and Al Bana is dominated by bubbling points. In contrast, at sites such as Dima and Al Hilayw where bubbling is rare or absent, outgassing is dominated by diffuse sources. We have not measured diffuse outgassing in Shumayt. Hence, total outgassing, and the contribution from diffuse sources, at Shumayt are unknown.

3.4 Outgassing rates from other sources

In addition to bubbling and diffuse outgassing in hyperalkaline pools, we measured flux rates of CH_4 on soils surrounding the bubbling springs and nearby non-alkaline streams. Results of field surveys are summarized in Supplementary Table S3.

CH_4 fluxes on soils surrounding hyperalkaline springs are almost too low to measure, with most values close to zero (see Supplemental Table 2). One case where we recorded significant CH_4 outgassing (53.5 mole CH_4 m^{-2} yr^{-1}) was in the partially submerged stream bank close to bubbling sources in Haylayn. We observed some bubbling beneath the sandy material along the stream bank. Thus, the high outgassing rates might be associated with a bubbling source. CH_4 outgassing in non-alkaline bodies of water (i.e., streams) close to hyperalkaline fluids is also small and hard to measure (at most 0.3 mole CH_4 m^{-2} yr^{-1}). Otherwise, results of all other observations in soils yield low values ranging -0.4 to 0.4 moles CH_4 m^{-2} yr^{-1}. Moreover, field observations yield high standard deviations that often exceed the flux values (see Supplemental Table 2). Taking this into account, it is difficult to measure outgassing (or ingassing) of CH_4 in soils surrounding hyperalkaline spring sites. In contrast, CH_4 flux in non-hyperalkaline streams and pools ($pH < 9$) proximate to hyperalkaline springs is mostly positive (*i.e.*, outgassing) but low (0.01 to 0.3 moles CH_4 m^{-2} yr^{-1}). Standard deviation of field experiments on non-alkaline fluids ranges from 7 to 50% of flux values.

With all this said, we caution that very small fluxes, approaching the detection limits of our measurement methods, could comprise a significant fraction of net outgassing if they occur over relatively large areas. Also, microbial consumption of H_2 and CH_4 and abiotic, near surface oxidation reactions could reduce surface fluxes relative to deeper production rates. It is evident that subsurface coalescence directs some fraction of diffusely produced gases to sites of focused outgassing, where microbial consumption and near-surface oxidation cannot keep pace with the flux of reduced gas. However, in areas where focusing mechanisms are weak or absent, a significant proportion of produced gas may be consumed before reaching the surface. For these reasons, in what follows, net fluxes estimated from our measurements should be viewed as minimum estimates of the rate of subsurface H_2 and CH_4 production.

4. Discussions

4.1 Ophiolites: Sink or source of greenhouse gas?

Carbon mineralization accompanying the serpentinization of ultramafic rocks like peridotites is considered an attractive setting for CO_2 sequestration strategies. Peridotites are enriched in divalent cations such as Mg^{+2} that favor formation of magnesium carbonates (e.g., magnesite) during reaction with CO_2-bearing fluids (Kelemen et al., 2011; Kelemen & Matter, 2008; National Academies of Sciences, Engineering, and Medicine, 2019). The accumulation of Ca^{+2} into increasingly alkaline fluids, from the dissolution of Ca-bearing pyroxenes (i.e., clinopyroxene) during serpentinization, create the potential for further removal of atmospheric CO_2 when highly alkaline fluids seep back to the surface and react with the atmosphere to form calcium carbonates (e.g., calcite). Overall, Kelemen & Matter (2008) estimated 10,000 – 100,000 metric tons CO_2 per year are sequestered via peridotite alteration in the Oman ophiolite.

CH_4, which is a greenhouse gas that has a 100-year global warming potential ~30 times more potent than CO_2 (IPCC, 2013), is actively outgassed in ophiolite settings. Outgassing of more than 300 – 3,000 metric tons of CH_4 per year could offset estimated CO_2 sequestration rates. If so, natural peridotite alteration in ophiolites could be a positive source of greenhouse warming potential. As shown in Table 4, focused and diffuse outgassing of CH_4 in bubbling and non-bubbling hyperalkaline pools in Haylayn can be up to 7,300 moles yr^{-1} which corresponds to 0.12 metric tons yr^{-1}. Other sites yield less outgassing of CH_4. There are more than a dozen sites that have been documented to host hyperalkaline springs (Chavagnac et al., 2013; Leong et al., 2021; Neal & Stanger, 1985; Paukert et al., 2012), and many more could remain undiscovered. However, even if there were ~ 100 hyperalkaline sites in the Oman ophiolite, with each outgassing methane at the same scale as Haylayn, the overall outgassing of 10 – 20 metric tons CH_4 yr^{-1} would be very low relative to the scale of CO_2 sequestration into solid minerals estimated by Kelemen & Matter (2008) in Oman.

Our field observations targeting outgassing in soils and non-alkaline water reveals little or no outgassing of CH_4 and hence are not likely to contribute to natural greenhouse emissions in the Oman ophiolite. Fractured peridotite outcrops, which were not explored in this work, are another potential source for CH_4 and H_2 outgassing in ophiolites. The recent work of Zgonnik et al. (2019) reported considerable diffuse outgassing of H_2 from altered and fractured serpentinized peridotites. The above work estimated H_2 outgassing from peridotite outcrops in the Oman ophiolite to range up to 2.2×10^6 moles km^{-2} yr^{-1} (or 150 m^3 day^{-1}). The H_2/CH_4 of gases sampled by Zgonnik et al. (2019) from outcrops ranges from 0.3 to 2 (~ 1). Therefore, CH_4 outgassing from outcrops in Oman can range up to 35 metric tons km^{-2} yr^{-1}. Given the outcrop area in Zgonnik et al.'s study area (~185 km^2) yields annual outgassing of hundreds of metric tons CH_4. If so, ongoing alteration of the Samail ophiolite may be greenhouse gas neutral. Extending the CH_4 flux reported by Zgonnik et al. to the total peridotite area of the Oman ophiolite (~5,500 km^2, 55% of the total ophiolite area of ~10,000 km^2, Nicolas et al., 2000) yields a CH_4 flux greater than 5,000 metric tons per year. If this is the case, the Oman ophiolite is an overall source for greenhouse gas.

However, Zgonnik et al. (2019) did not measure significant outgassing in relatively fresh outcrops and only recorded H_2 outgassing in more altered lithologies. Furthermore, Zgonnik et al. (2019) performed their flux experiments in shallow holes drilled into peridotite that may have tapped reduced gas that accumulates in fracture networks that is sourced over a much larger area. This is akin to hyperalkaline spring sites, where deep-seated fractures (probably faults and lithological boundaries) serve as conduits for coalescing discharge of deep-seated hyperalkaline fluids and reduced gases produced by diffuse alteration of a much larger rock volume. Thus, the maximum outgassing rates from Zgonnik et al. (2019) probably represent an upper bound on diffuse outgassing of CH_4.

In summary, it is not clear whether ongoing alteration of peridotite in the Samail ophiolite yields a net increase or a net reduction in greenhouse warming potential. However, proposed engineered methods to accelerate carbon mineralization in peridotite involve circulation of oxidized fluids (CO_2-rich water, “supercritical” CO_2), increasing fluid/rock ratios and subsurface oxygen fugacity (fO_2), and reducing the proportion of reduced gas production. Methane production in such settings is unlikely to significantly offset the effect of carbon mineralization in reducing greenhouse warming potential.

4.2 Isotopic constraints on sources of outgassed H_2 and CH_4

Results of noble gas isotopic analyses are summarized in Table 3 and shown in Figure 3b. Noble gas ratios ($^{20}Ne/^{4}He$ and R/R_a) of all gases sampled in this work plot close to that of an air end-member, as do a majority of previously analyzed samples from peridotite-hosted sources in Oman (Sano et al., 1993; Vacquand et al., 2018). Note that while the ratios indicate air-like signatures, the concentrations of atmospheric noble gases (^{20}Ne, ^{36}Ar, ^{84}Kr, ^{130}Xe) in study samples are significantly lower than air. This shows that the air-like signatures are not due air contamination, but rather an indicator of degassed air-saturated groundwater (i.e., dissolved gas stripped into bubbles when they formed), as illustrated in Supplementary Figure S1.

Because the highest accumulated H_2 concentrations in their experiments were observed in sedimentary rock units, rather than in the ophiolite, Zgonnik et al. (2019) proposed that H_2 in hyperalkaline springs in the Samail ophiolite could originate in the Pre-Cambrian to Paleozoic basement rocks and the Hawasina Formation underlying the ophiolite. Bubbling fluids seeping from these sedimentary sequences were previously sampled by Sano et al. (1993) and Vacquand et al. (2018). These fluids are less alkaline with pH < 11, N_2-dominated, and poor in H_2 and CH_4 (Figure 3a). They also contain a large component of crustal noble gases (Figure 3b). In contrast, most gas samples from ophiolite-hosted springs have noble gas signatures close to ambient air (this work, Sano et al., 1993; Vacquand et al., 2018) consistent with derivation via reaction of surface water with peridotite, and inconsistent with the hypothesis of Zgonnik et al. (2019).

Overall, H_2 and CH_4 seepage in hyperalkaline springs in ophiolites can originate from (1) abiotic or microbial reactions accompanying ongoing serpentinization, (2) decrepitation of ancient fluid inclusions that trapped previously formed high-temperature abiotic volatiles, and (3) sedimentary sequences beneath the ophiolite. Compositional and noble gas isotopic trends can help distinguish these sources. The CH_4/He and R/R_a trends of resulting mixtures of these three sources are plotted in Figure 5, together with the compositions of gases sampled in this work and Vacquand et al. (2018). The yellow diamond in Figure 5 depicts air-saturated water (ASW), characterized by low CH_4/He and R/R_a equal to one. Mixing of ASW with volatiles evolved during each of the above three processes are modeled and discussed next.

Input of H_2 and CH_4 generated during ongoing serpentinization into ASW yields the trend depicted by the black arrow in Figure 5, characterized by increasing CH_4/He ratios. CH_4 and H_2 are actively generated during water-rock reactions while He concentration is unchanged. Most of the gases sampled in this work plot along this trend.

Decrepitation of pre-existing and ancient fluid inclusions and liberation of CH_4 and H_2 hosted in these inclusions (Etiope et al., 2018; Grozeva et al., 2020; Klein et al., 2019; Luhmann et al., 2017; Miura et al., 2011) can add CH_4 and H_2 into modern groundwater. The composition and noble isotopic signatures of fluid inclusions hosted in Oman peridotites are unknown, but data exist for other sites. The CH_4 and noble gas composition (He, R/R_a) of fluid inclusions hosted in partially serpentinized peridotites from the Mid-Cayman Rise and Zambales ophiolite (Grozeva et al., 2020) are plotted as green squares in Figures 5a and 5b. Titration of gases mobilized from the fluid inclusion with the highest CH_4/He into ASW yields the trends depicted by the dashed green curve in Figure 5. Study samples plot along this mixing trend, which is flat before it curves up towards the observed data. Moreover, fluid inclusions formed during past submarine hydrothermal alteration of peridotite may contain noble gases derived mainly from seawater and would have R/R_a close to 1, indistinguishable from those in ASW and formed by ongoing peridotite alteration.

Mixing of ASW with gas from sediment-hosted springs, characterized by low CH_4/He ratios and R/R_a values, would result in the mixing trend depicted by the grey dashed curve in Figure 5a. None of the sampled fluids (various symbols in red) plots along this trend. Thus, most CH_4-rich (and H_2-rich) gases sampled in the ophiolite do not originate from the underlying sedimentary units. To summarize, the increasing CH_4/He and relatively constant R/R_a trend observed in our samples are more consistent with ongoing serpentinization sources. However, we cannot rule out contribution from ancient fluid inclusions based on existing data alone.

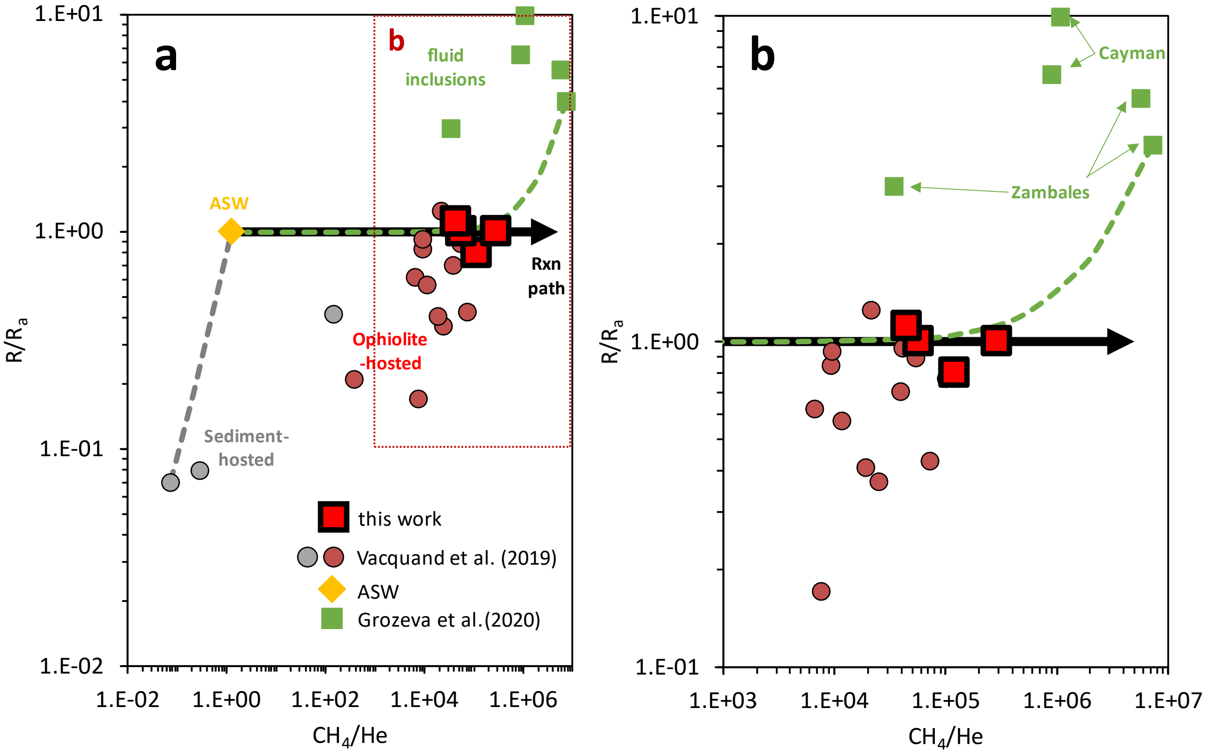

Figure 5. R/R_a and CH_4/He trends of samples collected in this work (bright red squares) and Vacquand et al. (2018) in red (taken from ophiolite-hosted springs) and grey (sediment-hosted springs) circles. (b) Enlarged view of the top right portion of (a), as indicated by the red dotted square in (a). Also included are results of fluid inclusion analysis by Grozeva et al. (2020) on peridotites from the Mid-Cayman Rise and Zambales ophiolite (green squares). Yellow diamond depicts air-saturated water (ASW). Black arrow indicates trend following input of CH_4 generated during active serpentinization of a peridotite reacted with a fluid with starting composition in equilibrium with air. Green dashed curve depicts input of CH_4 released from fluid inclusions typical of that found in the Zambales ophiolite sample with the highest CH_4/He to ASW. Grey dashed line depict input of sediment-hosted gas with the lowest CH_4/He and R/R_a into ASW.

4.3 Geochemical constraints on hydrocarbon sources

The geochemistry of short-chain alkanes (e.g., CH_4, C_2H_6, C_3H_8, C_4H_{10}) can help identify sources of outgassing, whether these volatiles are formed recently through biological reduction of inorganic or organic carbon substrates (microbial), high-temperature breakdown of organic matter (thermogenic), and high- or low-temperature abiogenic polymerization of C-H bonds (abiotic). As shown in Table 2, samples from all but one study sites have $CH_4/(C_2 + C_3)$ ratios that exceed 1000. High $CH_4/(C_2 + C_3)$ ratios are traditionally associated with microbial sources but recent works have shown that high $CH_4/(C_2 + C_3)$ values can also be found in hydrocarbons with thermogenic and abiotic origins (Milkov and Etiope, 2018). The highest ratio was measured on a sample from Shumayt, where results of a recent 16S rRNA gene sequencing work show that methanogens are predominant in springs in this site (Howells et al., 2022). Howells et al. (2022) show little to no evidence of methanogenesis at Dima where we measured lower $CH_4/(C_2 + C_3)$ ratios. The same work also shows that chemotrophic communities are dominated by methanogens at Al Bana. The microbial compositions of springs at Misfah, Al Hilayw, and Haylayn are yet to be determined. These findings show that microbial sources of CH_4 in our study sites are possible and that outgassed CH_4 can be young, consistent with detectable ^{14}C in CH_4 sampled from peridotite boreholes in Oman by Nothaft (2020). In addition to 16S rRNA gene sequences, deviation from equilibrium trends in clumped isotope ratios of CH_4 sampled from Oman boreholes further supports microbial sources (Nothaft et al., 2021b). While a thermogenic source for CH_4 from nearby sedimentary bodies is ruled out, Nothaft et al. (2021b) does not preclude high-temperature abiotic origins, including those released from fluid inclusion decrepitation, following measurements of enriched ^{13}C in ethane (C_2H_6) and propane (C_3H_8), similar to those measured on fluid inclusion-derived gases from oceanic lithospheric rocks.

The distribution of short-chain alkanes provides further clues on their sources. A logarithmic distribution of measured alkanes is shown in Supplementary Figure S2. Our results are consistent with previous findings by Boulart et al. (2013) for gas sampled from hyperalkaline springs in Oman (orange curves in Figure S2). Trends in Oman hydrocarbons deviate from the Schulz-Flory distribution, which is characterized by a strongly linear trend (in a log mole fraction vs C number plot) as exemplified by samples from Kidd Creek (green curves in Figure S2, Sherwood Lollar et al., 2002). This trend is typically associated with abiotic origins (Etiope & Sherwood Lollar, 2013). In contrast, trends observed from the Oman samples are more similar to those measured from Chimaera seeps in Turkey (blue curves in Figure S2) which is believed to have a predominantly low-temperature abiotic origin with some thermogenic input (Etiope et al., 2011). Note that the Oman gas samples are more enriched in CH_4 relative to heavier alkanes than those typical for thermogenic sources where the log mole fraction of C_{2+} alkanes are usually > -2.5 (Etiope & Sherwood Lollar, 2013). As follows, hydrocarbon data shown in this work are insufficient to trace sources of outgassing. Isotopic analyses, including radiocarbon ^{14}C, conventional $^{13}C_{CH4}$ and $^{2}H_{CH4}$, and clumped isotopes of a comprehensive set of samples in active hyperalkaline spring sites can further provide constraints on the contribution of recently formed CH_4, via active methanogenesis and/or present-day low-temperature abiotic polymerization reactions, to the total hydrocarbon outgassing in continental serpentinizing systems such as in Oman.

4.4 Estimating decrepitation and serpentinization rates from outgassing rates

As shown above, the gases in our samples could have been derived from active serpentinization (via low-temperature abiotic formation of H_2 and CH_4 or methanogenesis, i.e., microbial reduction of carbon sources to CH_4 using serpentinization-derived H_2) or mobilization from ancient fluid inclusions hosting volatiles previously formed during high-temperature abiogenesis. The rates of fluid inclusion decrepitation and serpentinization that account for observed outgassing rates were calculated. Results of calculations are presented in this section.

4.4.1 Rate of fluid inclusion decrepitation

Recent studies that quantified the amount of CH_4 hosted in fluid inclusions in a given mass of peridotite provide constraints on the mass or volume of rock that must contribute fluid inclusion-liberated volatiles, per unit time (decrepitation rate), to account for our observed outgassing rates, assuming all outgassed species originated in fluid inclusions (i.e., no modern abiotic or microbial sources). Serpentinized peridotites analyzed to date contain 0 – 360 micromoles CH_4 per kg rock (Etiope et al., 2018; Grozeva et al., 2020; Klein et al., 2019). Thus, a mole of CH_4

outgassed would require decrepitation of 2,800 kg or 0.9 m^3 of peridotite, assuming a CH_4 content of 360 micromoles kg^{-1} (Klein et al., 2019) and a rock density of 3000 kg m^{-3}. The volumes of rock required to decrepitate annually to account for our observed outgassing rates are reported in Table 5. For instance, gas from ~20 million kg of rock (or 6,800 m^3, see Table 5) is required to account for annual outgassing rates in Haylayn (7,300 moles CH_4 yr^{-1}, see Table 4). A possible decrepitation rate can also be constrained using measured H_2 outgassing rates. However, unlike CH_4, the amount of H_2 in fluid inclusions in a given mass of peridotite is less known.

Gabbros and chromitites have elevated CH_4 contents relative to serpentinized peridotites (Etiope et al., 2018; Grozeva et al., 2020). Input from these rocks would require less decrepitation to account for observed outgassing. Haylayn is located close to a peridotite-gabbro contact, and some of outgassed CH_4 (and H_2) might originate from nearby gabbros. However, peridotite outcrops are predominant upstream of the Haylayn site, and peridotites underlie gabbros downstream, so that fluids rising to the surface at Haylayn are likely to have reacted mainly with peridotite along subsurface pathways.

Table 5. Calculated decrepitation rates of fluid inclusion-bearing rock that would be required to account for the maximum measured outgassing rates.

Sites	**DECREPITATION RATE (m^3 rock yr^{-1})**
Haylayn	6,800
Al Banah	1,800
Shumayt	22
Dima	4,100
Misfah	2,800
Al Hilawy	110

Rates calculated assuming maximum value of 360 nmole CH_4 per gram rock measured by Klein et al. (2019). Rock density is assumed to be 3000 kg/m^3.

4.4.2 Serpentinization rates and constraints from thermodynamic reaction-path simulations

Aside from fluid inclusion decrepitation, outgassing could be a consequence of the ongoing serpentinization reactions that generate hyperalkaline fluids. H_2 is produced during serpentinization by the generalized reaction (1), in which a mole of H_2 is generated via reduction of H_2O coupled to oxidation of 2 moles of Fe(II) from primary (olivine and pyroxene) or secondary (Fe(II)-serpentine and brucite) phases to form Fe(III) in secondary minerals such as magnetite and Fe(III)-bearing serpentine. While reaction (1) illustrates an idealized scenario where the resulting Fe(III) is all in magnetite (Fe(III)/ΣFe = 0.67), analyses of natural serpentinites yield varying extents of oxidation, with Fe(III) hosted in a variety of minerals such as magnetite, andradite, and Fe(III)-bearing serpentine (Andreani et al., 2013; Ellison et al., 2021; Mayhew et al., 2018; Mayhew & Ellison, 2020; O'Hanley & Dyar, 1998; Templeton & Ellison, 2020; Tutolo et al., 2019, 2020). Using thermodynamic reaction path calculations, we simulate formation of these minerals during low-temperature, continental serpentinization of peridotite. Based on the average Fe(III)/ΣFe observed in ophiolite serpentinites (0.45, Mayhew and Ellison, 2020), we calculate production of 1 mole of H_2 during serpentinization of ~3.5 kg of peridotite (Figures S3c). This result is different from the estimate based on the assumption that all Fe(III) is hosted in magnetite (1 mole H_2 per ~2 kg peridotite). Details on these model results are found in the supporting section.

The serpentinization rate (m^3 rock yr^{-1}) required to account for measured outgassing rates shown in Table 4 are reported in Table 6, assuming low temperature serpentinization of ~3.5 kg of peridotite is required to generate 1 mole of H_2. This translates into 0.3 mole H_2 generated per kg of rock altered or 900 moles H_2 per m^3 of peridotite, assuming a density of 3,000 kg m^{-3}. Outgassed H_2 and CH_4 (converted to H_2 units by a factor of 4 via reaction 2) were considered in calculating these reaction rates. For example, outgassing of CH_4 (7,300 moles yr^{-1}) and H_2

(79,000 moles yr^{-1}) at Haylayn requires reaction of 34 and 92 m^3 peridotite yr^{-1}, respectively, yielding a total of ~130 m^3 yr^{-1} as shown in Table 6. This is 50 times smaller than the volume of rock (~6,800 m^3 yr^{-1}, Table 5) required to yield the same gas fluxes via fluid inclusion decrepitation.

Table 6. Calculated serpentinization rates that would be required to account for the maximum measured CH_4, H_2, and total (CH_4 + H_2) outgassing rates.

	REACTION RATE (m^3 rock yr^{-1})		
Sites	**CH_4**	**H_2**	**SUM**
Haylayn	34	92	130
Al Banah	9.2	34	44
Shumayt	0.1	1.2	1.3
Dima	20	0.8	21
Misfah	14	32	46
Al Hilayw	0.6	1.4	2.0

4.5 Comparison of field-derived rates with laboratory rates

Serpentinization rates calculated above in m^3 yr^{-1} can be converted into mass or volume fraction rates (sec^{-1}) and compared to rates estimated from the results of laboratory experiments. To derive volume fraction rates, the volume (m^3) of the subsurface reaction zone must be estimated. An effective catchment area of 25 km^2 was estimated by Dewandel et al. (2005) for Wadi Khafifah, which is a watershed hosting hyperalkaline spring sites in Oman that is close to study sites Dima and Misfah. Dewandel et al. (2005) also noted that hyperalkaline flows were observed in sites where the catchment area is only ~1 km^2. Dewandel et al. (2005) estimated hyperalkaline flows to originate deeper than 500 m. Thus, the volume of peridotite that interacted with meteoric-derived water to generate H_2- and CH_4-rich hyperalkaline fluids could range from 0.5 to 12.5 km^3 (1 to 25 km^2 * 0.5 km). More recent work has shown that hyperalkaline fluids are present at depths as shallow as 50 m (Kelemen et al., 2020; 2021; Miller et al., 2016; Nothaft et al., 2021a; 2021b; Paukert et al., 2012; Paukert Vankeuren et al., 2019;

Rempfert et al., 2017; Templeton et al., 2021). Consequently, the reaction zone volume could be at least 0.05 km^3 (1 km^2 * 0.05 km).

Note that the above reaction zone volume is not the amount of rock that reacted annually. Reaction only occurs where fluids can interact with aquifer host rocks, as in pores and in fractures. As shown in Table 4, a maximum of 130 m^3 of rock (i.e., the annual reacted volume for Haylayn) distributed in the abovementioned volumes of rock in the subsurface reaction zone react with fluids annually. Assuming reaction zone volumes ranging from 0.05 to 12.5 km^3, a reaction rate of 130 m^3 yr^{-1} calculated to account for outgassing in Haylayn would yield volume fraction rate ranging from $3x10^{-16}$ to $8x10^{-14}$ sec^{-1}. Rates calculated for Haylayn as well as other study sites are shown in Figure 6 (various green arrows). These rates are compared to temperature-rate fits (dashed curves) determined from results of high-temperature laboratory experiments as well as other rates calculated for other sites of serpentinization in Figure 6a. The high-temperature laboratory experiments where the fits are based on are shown in Figure 6b. The dashed red curves are temperature fits calculated by Kelemen & Matter (2008) from the experimental data of Martin & Fyfe (1970). These fits were modified from equation 3 of Kelemen and Matter (2008) to account for varying surface areas for grain sizes different than those used in the experiments of Martin and Fyfe (~60 micrometer). An extended low-temperature fit derived by Malvoisin et al. (2012) from their high-temperature experiments (38-50 micrometer grain size) is represented by the dashed blue curve. Lamadrid et al. (2021) calculated surface area-dependent low-temperature fits from their high-temperature (>150 °C) experimental results. These are depicted in Figure 6 by several dashed grey curves representing high (1 micrometer grain size or fracture spacing) to low (1 meter grain size or fracture spacing) reactive surfaces. Note that low-temperature fits shown in Figure 6a are derived from high-temperature experiments (>150 °C, Figure 6b) and a low-temperature rate is yet to be determined directly from laboratory experiments owing to limits in quantifying slow reaction progress at low temperatures. In the absence of laboratory data, preliminary constraints on low-temperature serpentinization rates can be determined using field data collected in this work. Rates derived from our field sites (various green arrows, Figure 6a) plot lower than the empirically-derived fits of Malvoisin et al. (2012), Lamadrid et al. (2021), and Kelemen and Matter (2008) for high reactive surface areas (<1 mm grain size). In contrast, the field-determined rates are consistent with those calculated by Lamadrid et al. (2021) and Kelemen & Matter (2008) for the low reactive surface area expected in peridotite-hosted continental aquifers such as in Oman (~meter scale fracture spacing, Kelemen et al., 2011).

Estimated serpentinization rates calculated by Früh-Green et al. (2003) for the Atlantis Massif, which hosts the Lost City Hydrothermal Field are shown with the blue field in Figure 6a, based on 20 wt% serpentinization over 30,000 to 1.5 million years. The temperature range of the blue field in Figure 6a is based on the temperatures of Lost City vent fluids (40 – 120 °C, Kelley et al., 2001; Seyfried et al., 2015) but might extend to higher temperature in the root of the hydrothermal system beneath Lost City (~200 °C, Seyfried et al., 2015), hence the arrow. Overall, serpentinization rates estimated for the Atlantis Massif system are consistent with those extrapolated from high-temperature experiments assuming low reactive surface area.

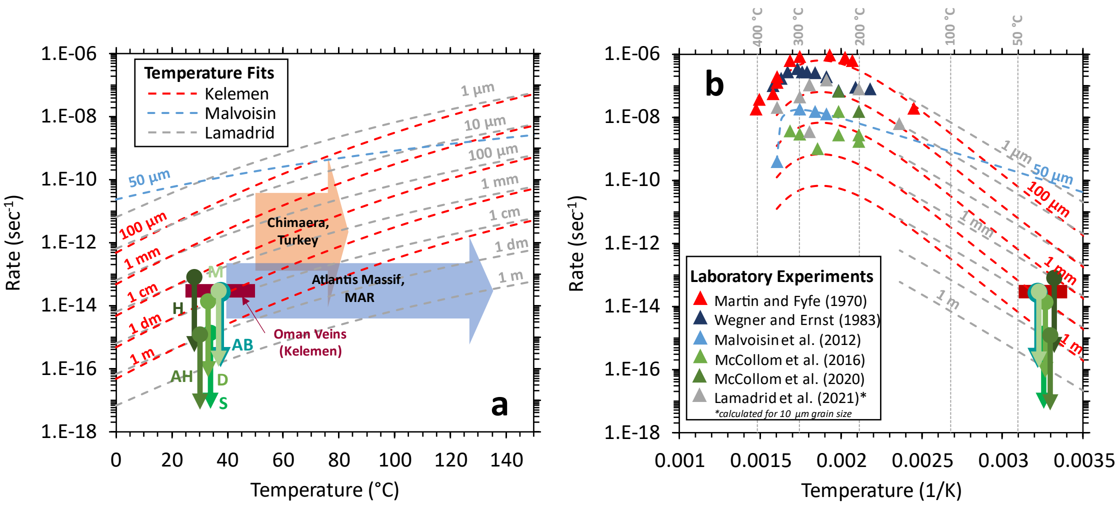

Figure 6. (a) Comparison of field-determined serpentinization rates (this work and others) with temperature-rate fits to results of high-temperature laboratory experiments. These fits were derived by Kelemen and Matter (2008, red dashed curves, accounting for varying surface areas for different grain sizes from the data of Martin and Fyfe, 1970), and by Malvoisin et al. (2012, dashed blue curve) and Lamadrid et al. (2021, dashed grey curve for various indicated surface area or fracture spacing) from their own experimental data. Blue arrow represents rates estimated by Früh-Green et al. (2003) for Atlantis Bank. Orange arrow represents rates based on outgassing in the Chimaera seeps in Turkey measured by Etiope et al. (2011). Red rectangle shows the rate calculated by Kelemen et al. (2021) using the volume of young serpentine veins, that cut young carbonate veins in drill cores from the Samail ophiolite. Various green arrows depict rates derived from outgassing rates in different study sites (AH – Al Hilayw; AB – Al Bana; D – Dima; H – Haylayn; M – Misfah; S – Shumayt). Circles at top of arrows indicate maximum serpentinization rates calculated from maximum outgassing rates and minimum reaction zone volume (0.05 km^3). The downward arrow depicts rates corresponding to lower outgassing rates measured at each site and larger assumed reaction zone volumes (up to 12.5 km^3). (b) Similar to (a) but temperature in 1/K and includes rates determined in several high-temperature laboratory experiments (triangles in various colors, (Martin and Fyfe, 1970; Wegner and Ernst, 1983; Malvoisin et al., 2012; McCollom et al., 2016, 2020; Lamadrid et al., 2021)). Data shown in grey triangles are values calculated by Lamadrid et al. from their own experimental data for reactants with 10 micrometer grain sizes.

Some of the largest observed outgassing of abiotic CH_4 occurs in the Chimaera seeps in Turkey where Etiope et al. (2011) estimated outgassing of 12 million moles CH_4 yr^{-1}. H_2 outgassing rates at Chimaera were not measured. H_2/CH_4 ratios of 0.1 to 0.125 (Etiope et al., 2011) indicate that H_2 outgassing should be at least 10 times less (~1.2 million moles H_2 yr^{-1}) than CH_4 outgassing. Assuming that H_2 and CH_4 are generated during present-day serpentinization, and considering reaction volume of 0.05 to 12.5 km^3, a rate of 1x10^{-13} to 4x10^{-11} sec^{-1} is required to account for reduced gas outgassing in Chimaera. As depicted by the orange arrow in Figure 6a, such a rate would probably require large reactive surface areas. Additional methane can be source from decrepitation of fluid inclusions or a hotter subsurface reaction zone. The low deuterium/hydrogen isotopic ratio of H_2 outgassed at Chimaera suggests a low-temperature origin (<50 °C) (Etiope et al., 2011). However, recent isotopologue analysis (Young et al., 2017; Douglas et al., 2017) of CH_4 outgassed in Chimaera suggests a higher temperature origin (>100 °C). While believed to be dominantly abiotic, isotopic work indicate mixing of minor amounts of thermogenic CH_4 that may be sourced from sediments underlying ultramafic rocks (Etiope et al., 2011). Alternatively, higher temperature formation temperatures of reduced gases at Chimaera could have been recorded by fluid inclusions generated during past hydrothermal alteration. However, following the reasoning outlined in Section 4.3, derivation of 12 million moles CH_4 yr^{-1} would require decrepitation of fluid inclusions in >10 million m^3 of rock yr^{-1}, or more than 20 km^3 over the inferred minimum of 2000 years of methane outgassing at Chimaera, which has been active since the Hellenistic period (i.e., site of the first Olympic Fire, Hosgormez et al., 2008).

The high end of the Haylayn, Al Bana, and Misfah rate estimates (up to $8x10^{-14}$ sec^{-1}) are consistent with an order of magnitude estimate derived by Kelemen et al. (2021). Analyzing drill cores from serpentinized peridotite in the Samail ophiolite, Kelemen et al. found that 23 of 35 samples of carbonate veins contained appreciable ^{14}C. In turn, these carbonate veins, containing a relatively young carbon component, are intergrown with or cut by a generation of “waxy serpentine” veins comprising a few percent of the drill cores. These data yield an order of magnitude serpentinization rate of 1 volume percent per 10,000 years, or (assuming no large density contrasts) a mass fraction rate of $3x10^{-14}$ sec^{-1} as shown by the red rectangle in Figure 6. Note that, based on cross-cutting relationships, these late “waxy” serpentine veins are the youngest set of veins in the core, and are not representative of previous generations of serpentine veins observed from the Oman ophiolite (Kelemen et al., 2021). Older generations of serpentine veins and “mesh cores” might have formed at current or higher temperature conditions, and may have replaced earlier mineral assemblages at a faster or slower rate. These variations in serpentine formation may yield variable H_2 production and ultimately, variable outgassing rates.

4.6 Extent of active serpentinization and fluid inclusion decrepitation

The above calculations place constraints on the extent of active serpentinization and/or fluid inclusion decrepitation required to account for active outgassing of H_2 and CH_4 in hyperalkaline spring sites. Only a small volume of rock (130 m^3, see Table 6) must be altered per year to account for active outgassing at Haylayn, the site which has the highest outgassing rates measured for peridotite-hosted sites in the Samail ophiolite. In contrast, all of the fluid inclusions in an estimated ~6,800 m^3 of rock per year (Table 5) need to be decrepitated to account for observed outgassing at Haylayn. Ultimately, for outgassing rates at Haylayn, fluid inclusions stored in one cubic kilometer of peridotite would be exhausted after ~150,000 years. Normalizing for every km^2 area extent of exposed peridotite, this would result in the advance of a serpentinization or alteration front at 6.8×10^{-6} km yr^{-1}. This is 20 times faster than regional uplift rates of 0.3 mm yr^{-1} or 0.3×10^{-6} km yr^{-1} for the Oman mountains (Poupeau et al., 1998). Thus, if uplift is negligible, – and if the velocity of the serpentinization front were constant over time –, the front would have advanced beyond the maximum thickness of the peridotite in the Samail ophiolite (~ 5 km; Ravaut et al., 1997) in 740,000 years.

5. Conclusions

This work showed that outgassing of reduced gases (H_2 and CH_4) in serpentinization-generated hyperalkaline spring sites in the Samail ophiolite in Oman is variable. Quiescent sites annually outgassed ~100 and ~1,000 moles of CH_4 and H_2, respectively. In contrast, more vigorous sites yield yearly outgassing amounting to ~7,000 and 70,000 moles CH_4 and H_2, respectively. While hyperalkaline sites are sources of greenhouse emissions (i.e., CH_4), total spring-related CH_4 outgassing in the entire Samail ophiolite is still far lower than the amount of CO_2 estimated to be sequestered into the ophiolite through carbon mineralization reactions. However, outgassing from soils and outcrops surrounding hyperalkaline springs remained unconstrained. Our field experiments show no to little outgassing from soils and outcrops, yet it is likely that our instrumentation is not sensitive enough to measure small changes in gas concentrations over limited time constraints in the field. Ultimately, future surveys that can uncover and map gas seeps in soils and outcrops and determine their outgassing rates would provide a more comprehensive quantification of the total reduced volatile budget and flux in the entire Samail ophiolite.

Compositional and noble gas isotopic constraints reveal that H_2 and CH_4 outgassed in study sites are derived from either active serpentinization or from the decrepitation of fluid inclusions that host H_2 and CH_4 formed from previous high-temperature water-rock interactions. Further analysis such as determining the age of CH_4 through ^{14}C analysis and their clumped isotopic compositions can help distinguished whether reduced gases in serpentinizing sites in Oman are formed actively at present-day ambient conditions, either abiotically or microbially, or during previous high-temperature serpentinization. Stable isotopic work that can fingerprint gases stored in mineral-hosted fluid inclusions in ultramafic and gabbroic rocks in the Samail ophiolite can help future mixing calculations that will quantify extents of each end-member sources on present-day outgassing in Oman.

Active serpentinization rates were calculated assuming outgassed H_2 and CH_4 are formed via modern processes. Calculated rate ranges from 8×10^{-14} sec^{-1} to much lower values, consistent with very slow rates expected at low temperatures as well as recent estimates from analysis of the extents and age of carbonation in peridotite cores recently drilled from the Samail ophiolite (Kelemen et al., 2021). These findings show that present-day serpentinization can account for active volatile outgassing in hyperalkaline springs. However, this does not rule out contribution from volatiles mobilized via fluid inclusion decrepitation. Though for fluid inclusion decrepitation to sustain similar outgassing rates for a long period of time, gas must be sourced from at least 20 times more volume of rock, and the serpentinization rate in this volume must be unusually high compared to most of the area of exposed peridotite in the Samail ophiolite. Methods that can decipher movement of fluids and gases in subsurface fractures in the Samail ophiolite can help inform if present-day outgassing and spring discharge can be indeed sourced from such a wide area.

Serpentinization is a widespread process. It can occur whenever and wherever ultramafic rocks and water meet, such as in various ophiolitic and orogenic bodies emplaced on Earth's continents, uplifted ultramafic rocks in the seafloor, and in other rocky bodies in our solar system such as Mars and the Ocean Worlds. Overall, our findings show that the rate of volatile outgassing can help quantify subsurface reactions rates accompanying serpentinization in various low-temperature settings on Earth and perhaps, in other rocky bodies beyond our planet. These rates operate at geologically short timescales and can have profound implications on the habitability of rock-hosted environments and the supply of reduced volatiles to the atmosphere.

6. Acknowledgements

We would like to thank Martin Stute for assistance and training in field gas sampling, Everett Shock for lending field instruments, and Ben Tutolo and two anonymous reviewers for insightful and constructive reviews that substantially improved the final paper. Discussions in the field with the Oman Drilling Project team was also helpful and insightful. Support from the Storke Memorial Endowment fund to Peter Kelemen is acknowledged.

7. Appendix A: Supplementary Materials

Supplementary Material 1 includes supplementary figures 1 to 4, as well as a section that discusses the thermodynamic constraints on H_2 production during low-temperature serpentinization. Supplementary Tables 1, 2, and 3 are uploaded separately as csv files.

8. References

Abrajano T. A., Sturchio N. C., Bohlke J. K., Lyon G. L., Poreda R. J. and Stevens C. M. (1988) Methane-hydrogen gas seeps, Zambales Ophiolite, Philippines: Deep or shallow origin? *Chem. Geol.* **71**, 211–222.

Andreani M., Muñoz M., Marcaillou C. and Delacour A. (2013) µXANES study of iron redox state in serpentine during oceanic serpentinization. *Lithos* **178**, 70–83.

Barnes I., LaMarche V. C. and Himmelberg G. (1967) Geochemical evidence of present-day serpentinization. *Science* **156**, 830–832.

Barry P. H., Lawson M., Meurer W. P., Warr O., Mabry J. C., Byrne D. J. and Ballentine C. J. (2016) Noble gases solubility models of hydrocarbon charge mechanism in the Sleipner Vest gas field. *Geochim. Cosmochim. Acta* **194**, 291–309.

Berndt M. E., Allen D. E. and Seyfried W. E. Jr (1996) Reduction of CO_2 during serpentinization of olivine at 300 °C and 500 bar. *Geology* **24**, 351–354.

Berner E. K. and Berner R. A. (2012) *Global Environment: Water, air, and geochemical Cycles.*, Princeton University Press.

Blackwell D. D. (1971) The thermal structure of the continental crust. In *The structure and physical properties of the earth's crust* (ed. J. G. Heacock). Geophysical Monograph Series. Symposium on the Structure and Physical Properties of the Earth's Crust. American Geophysical Union, Washington.

Boulart C., Chavagnac V., Monnin C., Delacour A., Ceuleneer G. and Hoareau G. (2013) Differences in gas venting from ultramafic-hosted warm springs: The example of Iman and Voltri Ophiolites. *Ofioliti* **38**, 142–156.

Byrne D. J., Barry P. H., Lawson M. and Ballentine C. J. (2018) Determining gas expulsion vs retention during hydrocarbon generation in the Eagle Ford Shale using noble gases. *Geochim. Cosmochim. Acta* **241**, 240–254.

Canovas P. A., Hoehler T. and Shock E. L. (2017) Geochemical bioenergetics during low-temperature serpentinization: An example from the Samail ophiolite, Sultanate of Oman: Serpentinization Bioenergetics. *J. Geophys. Res. Biogeosciences* **122**, 1821–1847.

Chavagnac V., Monnin C., Ceuleneer G., Boulart C. and Hoareau G. (2013) Characterization of hyperalkaline fluids produced by low-temperature serpentinization of mantle peridotites in the Oman and Ligurian ophiolites: Hyperalkaline Waters in Oman and Liguria. *Geochem. Geophys. Geosystems* **14**, 2496–2522.

Crespo-Medina M., Twing K. I., Sánchez-Murillo R., Brazelton W. J., McCollom T. M. and Schrenk M. O. (2017) Methane dynamics in a tropical serpentinizing environment: The Santa Elena Ophiolite, Costa Rica. *Front. Microbiol.* **8**, no. 916.

D'Alessandro W., Daskalopoulou K., Calabrese S. and Bellomo S. (2018) Water chemistry and abiogenic methane content of a hyperalkaline spring related to serpentinization in the Argolida ophiolite (Ermioni, Greece). *Mar. Pet. Geol.* **89**, 185–193.

Darrah T. H., Jackson R. B., Vengosh A., Warner N. R., Whyte C. J., Walsh T. B., Kondash A. J. and Poreda R. J. (2015) The evolution of Devonian hydrocarbon gases in shallow aquifers of the northern Appalachian Basin: Insights from integrating noble gas and hydrocarbon geochemistry. *Geochim. Cosmochim. Acta* **170**, 321–355.

Dewandel B., Lachassagne P., Boudier F., Al-Hattali S., Ladouche B., Pinault J.-L. and Al-Suleimani Z. (2005) A conceptual hydrogeological model of ophiolite hard-rock aquifers in Oman based on a multiscale and a multidisciplinary approach. *Hydrogeol. J.* **13**, 708–726.

Douglas P. M. J., Stolper D. A., Eiler J. M., Sessions A. L., Lawson M., Shuai Y., Bishop A., Podlaha O. G., Ferreira A. A., Santos Neto E. V., Niemann M., Steen A. S., Huang L., Chimiak L., Valentine D. L., Fiebig J., Luhmann A. J., Seyfried W. E., Etiope G., Schoell M., Inskeep W. P., Moran J. J. and Kitchen N. (2017) Methane clumped isotopes: Progress and potential for a new isotopic tracer. *Org. Geochem.* **113**, 262–282.

Ellison E. T., Templeton A. S., Zeigler S. D., Mayhew L. E., Kelemen P. B., Matter J. M. and Party T. O. D. P. S. (2021) Low-temperature hydrogen formation during aqueous alteration of serpentinized peridotite in the Samail ophiolite. *J. Geophys. Res. Solid Earth* **126**, e2021JB021981.

Etiope G., Ifandi E., Nazzari M., Procesi M., Tsikouras B., Ventura G., Steele A., Tardini R. and Szatmari P. (2018) Widespread abiotic methane in chromitites. *Sci. Rep.* **8**, 8728.

Etiope G., Samardžić N., Grassa F., Hrvatović H., Miošić N. and Skopljak F. (2017) Methane and hydrogen in hyperalkaline groundwaters of the serpentinized Dinaride ophiolite belt, Bosnia and Herzegovina. *Appl. Geochem.* **84**, 286–296.

Etiope G., Schoell M. and Hosgörmez H. (2011) Abiotic methane flux from the Chimaera seep and Tekirova ophiolites (Turkey): Understanding gas exhalation from low temperature serpentinization and implications for Mars. *Earth Planet. Sci. Lett.* **310**, 96–104.

Etiope G. and Sherwood Lollar B. (2013) Abiotic Methane on Earth. *Rev. Geophys.* **51**, 276–299.

Etiope G., Tsikouras B., Kordella S., Ifandi E., Christodoulou D. and Papatheodorou G. (2013) Methane flux and origin in the Othrys ophiolite hyperalkaline springs, Greece. *Chem. Geol.* **347**, 161–174.

Falk E. S., Guo W., Paukert A. N., Matter J. M., Mervine E. M. and Kelemen P. B. (2016) Controls on the stable isotope compositions of travertine from hyperalkaline springs in Oman: Insights from clumped isotope measurements. *Geochim. Cosmochim. Acta* **192**, 1–28.

Früh-Green G. L., Kelley D. S., Bernasconi S. M., Karson J. A., Ludwig K. A., Butterfield D. A., Boschi C. and Proskurowski G. (2003) 30,000 years of hydrothermal activity at the Lost City Vent Field. *Science* **301**, 495–498.

Glein C. R. and Zolotov M. Y. (2020) Hydrogen, hydrocarbons, and habitability across the solar system. *Elements* **16**, 47–52.

Goff F. and Lackner K. S. (1998) Carbon dioxide sequestering using ultramafic rocks. *Environ. Geosci.* **5**, 89–101.

Grozeva N. G., Klein F., Seewald J. S. and Sylva S. P. (2020) Chemical and isotopic analyses of hydrocarbon-bearing fluid inclusions in olivine-rich rocks. *Philos. Trans. R. Soc. Math. Phys. Eng. Sci.* **378**, 20180431.

Hanghøj K., Kelemen P. B., Hassler D. and Godard M. (2010) Composition and genesis of depleted mantle peridotites from the Wadi Tayin Massif, Oman Ophiolite; Major and trace element geochemistry, and Os isotope and PGE systematics. *J. Petrol.* **51**, 201–227.

Horita J. and Berndt M. E. (1999) Abiogenic methane formation and isotopic fractionation under hydrothermal conditions. *Science* **285**, 1055–1057.

Hosgormez H., Etiope G. and Yalçin M. N. (2008) New evidence for a mixed inorganic and organic origin of the Olympic Chimaera fire (Turkey): a large onshore seepage of abiogenic gas. *Geofluids* **8**, 263–273.

Howells A. E. G., Leong J. A. M., Ely T., Santana M., Robinson K., Esquivel-Elizondo S., Cox A., Poret-Peterson A., Krajmalnik-Brown R. and Shock E. L. (2022) Energetically informed niche models of hydrogenotrophs detected in sediments of serpentinized fluids of the Samail ophiolite of Oman. *J. Geophys. Res. Biogeosciences* **127**.

Hutchinson G. L. and Mosier A. R. (1981) Improved soil cover method for field measurement of nitrous oxide fluxes. *Soil Sci. Soc. Am. J.* **45**, 311–316.

Kelemen P. B., Leong J. A., Carlos de Obeso J., Matter J. M., Ellison E. T., Templeton A., Nothaft D. B., Eslami A., Evans K., Godard M., Malvoisin B., Coggon J. A., Warsi N. H., Pézard P., Choe S., Teagle D. A. H., Michibayashi K., Takazawa E., Al Sulaimani Z. and Team T. O. D. P. S. (2021) Initial results From the Oman Drilling Project Multi-Borehole Observatory: Petrogenesis and ongoing alteration of mantle peridotite in the weathering horizon. *J. Geophys. Res. Solid Earth* **126**, e2021JB022729.

Kelemen P. B. and Matter J. (2008) In situ carbonation of peridotite for CO_2 storage. *Proc. Natl. Acad. Sci.* **105**, 17295–17300.

Kelemen P.B., Matter J. M., Teagle D. A. H., Coggon J. A., and Oman Drilling Project Science Team eds. (2020) *Scientific Drilling in the Samail Ophiolite, Sultanate of Oman.*, International Ocean Discovery Program.

Kelemen P. B., Matter J., Streit E. E., Rudge J. F., Curry W. B. and Blusztajn J. (2011) Rates and mechanisms of mineral carbonation in peridotite: Natural processes and recipes for enhanced, in situ CO_2 capture and storage. *Annu. Rev. Earth Planet. Sci.* **39**, 545–576.

Kelemen P. B., McQueen N., Wilcox J., Renforth P., Dipple G. and Vankeuren A. P. (2020) Engineered carbon mineralization in ultramafic rocks for CO_2 removal from air: Review and new insights. *Chem. Geol.* **550**, 119628.

Kelley D. S., Karson J. A., Blackman D. K., Früh-Green G. L., Butterfield D. A., Lilley M. D., Olson E. J., Schrenk M. O., Roe K. K., Lebon G. T., Rivizzigno P. and the AT3-60 Shipboard Party (2001) An off-axis hydrothermal vent field near the Mid-Atlantic Ridge at 30° N. *Nature* **412**, 145–149.

Klein F., Bach W., Humphris S. E., Kahl W.-A., Jöns N., Moskowitz B. and Berquó T. S. (2014) Magnetite in seafloor serpentinite—Some like it hot. *Geology* **42**, 135–138.

Klein F., Bach W., Jöns N., McCollom T., Moskowitz B. and Berquó T. (2009) Iron partitioning and hydrogen generation during serpentinization of abyssal peridotites from 15°N on the Mid-Atlantic Ridge. *Geochim. Cosmochim. Acta* **73**, 6868–6893.

Klein F., Grozeva N. G. and Seewald J. S. (2019) Abiotic methane synthesis and serpentinization in olivine-hosted fluid inclusions. *Proc. Natl. Acad. Sci.* **116**, 17666–17672.

Kohl L., Cumming E., Cox A., Rietze A., Morrissey L., Lang S. Q., Richter A., Suzuki S., Nealson K. H. and Morrill P. L. (2016) Exploring the metabolic potential of microbial communities in ultra-basic, reducing springs at The Cedars, CA, USA: Experimental evidence of microbial methanogenesis and heterotrophic acetogenesis. *J. Geophys. Res. Biogeosciences* **121**, 1203–1220.

Lamadrid H. M., Zajacz Z., Klein F. and Bodnar R. J. (2021) Synthetic fluid inclusions XXIII. Effect of temperature and fluid composition on rates of serpentinization of olivine. *Geochim. Cosmochim. Acta* **292**, 285–308.

Lee J.-Y., Marti K., Severinghaus J. P., Kawamura K., Yoo H.-S., Lee J. B. and Kim J. S. (2006) A redetermination of the isotopic abundances of atmospheric Ar. *Geochim. Cosmochim. Acta* **70**, 4507–4512.

Leong J. A. M., Howells A. E., Robinson K. J., Cox A., Debes R. V., Fecteau K., Prapaipong P. and Shock E. L. (2021) Theoretical predictions versus environmental observations on serpentinization fluids: Lessons from the Samail ophiolite in Oman. *J. Geophys. Res. Solid Earth* **126**, e2020JB020756.

Leong J. A. M. and Shock E. L. (2020) Thermodynamic constraints on the geochemistry of low-temperature, continental, serpentinization-generated fluids. *Am. J. Sci.* **320**, 185–235.

Luhmann A. J., Tutolo B. M., Bagley B. C., Mildner D. F. R., Scheuermann P. P., Feinberg J. M., Ignatyev K. and Seyfried W. E. (2017) Chemical and physical changes during seawater flow through intact dunite cores: An experimental study at 150–200°C. *Geochim. Cosmochim. Acta* **214**, 86–114.

Malvoisin B., Brunet F., Carlut J., Rouméjon S. and Cannat M. (2012) Serpentinization of oceanic peridotites: 2. Kinetics and processes of San Carlos olivine hydrothermal alteration. *J. Geophys. Res. Solid Earth* **117**.

Martin B. and Fyfe W. S. (1970) Some experimental and theoretical observations on the kinetics of hydration reactions with particular reference to serpentinization. *Chem. Geol.* **6**, 185–202.

Matter J. M. and Kelemen P. B. (2009) Permanent storage of carbon dioxide in geological reservoirs by mineral carbonation. *Nat. Geosci.* **2**, 837–841.

Mayhew L. E. and Ellison E. T. (2020) A synthesis and meta-analysis of the Fe chemistry of serpentinites and serpentine minerals. *Philos. Trans. R. Soc. Math. Phys. Eng. Sci.* **378**, 20180420.

Mayhew L. E., Ellison E. T., McCollom T. M., Trainor T. P. and Templeton A. S. (2013) Hydrogen generation from low-temperature water–rock reactions. *Nat. Geosci.* **6**, 478–484.

Mayhew L. E., Ellison E. T., Miller H. M., Kelemen P. B. and Templeton A. S. (2018) Iron transformations during low temperature alteration of variably serpentinized rocks from the Samail ophiolite, Oman. *Geochim. Cosmochim. Acta* **222**, 704–728.

McCollom T. M. (2016) Abiotic methane formation during experimental serpentinization of olivine. *Proc. Natl. Acad. Sci.* **113**, 13965–13970.

McCollom T. M. and Donaldson C. (2016) Generation of hydrogen and methane during experimental low-temperature reaction of ultramafic rocks with water. *Astrobiology* **16**, 389–406.

McCollom T. M., Klein F., Robbins M., Moskowitz B., Berquó T. S., Jöns N., Bach W. and Templeton A. (2016) Temperature trends for reaction rates, hydrogen generation, and partitioning of iron during experimental serpentinization of olivine. *Geochim. Cosmochim. Acta* **181**, 175–200.

McCollom T. M., Klein F., Solheid P. and Moskowitz B. (2020) The effect of pH on rates of reaction and hydrogen generation during serpentinization. *Philos. Trans. R. Soc. Math. Phys. Eng. Sci.* **378**, 20180428.

McCollom T. M. and Seewald J. S. (2007) Abiotic synthesis of organic compounds in deep-sea hydrothermal environments. *Chem. Rev.* **107**, 382–401.

McCollom T. M. and Seewald J. S. (2003) Experimental constraints on the hydrothermal reactivity of organic acids and acid anions: I. Formic acid and formate. *Geochim. Cosmochim. Acta* **67**, 3625–3644.

McDermott J. M., Seewald J. S., German C. R. and Sylva S. P. (2015) Pathways for abiotic organic synthesis at submarine hydrothermal fields. *Proc. Natl. Acad. Sci.* **112**, 7668–7672.

Mervine E. M., Humphris S. E., Sims K. W. W., Kelemen P. B. and Jenkins W. J. (2014) Carbonation rates of peridotite in the Samail Ophiolite, Sultanate of Oman, constrained through 14C dating and stable isotopes. *Geochim. Cosmochim. Acta* **126**, 371–397.

Milkov A. V. and Etiope G. (2018) Revised genetic diagrams for natural gases based on a global dataset of >20,000 samples. *Org. Geochem.* **125**, 109–120.

Miller H. M., Matter J. M., Kelemen P., Ellison E. T., Conrad M. E., Fierer N., Ruchala T., Tominaga M. and Templeton A. S. (2016) Modern water/rock reactions in Oman hyperalkaline peridotite aquifers and implications for microbial habitability. *Geochim. Cosmochim. Acta* **179**, 217–241.

Miura M., Arai S. and Mizukami T. (2011) Raman spectroscopy of hydrous inclusions in olivine and orthopyroxene in ophiolitic harzburgite: Implications for elementary processes in serpentinization. *J. Mineral. Petrol. Sci.* **106**, 91–96.

Monnin C., Quéméneur M., Price R., Jeanpert J., Maurizot P., Boulart C., Donval J.-P. and Pelletier B. (2021) The Chemistry of Hyperalkaline Springs in Serpentinizing Environments: 1. The Composition of Free Gases in New Caledonia Compared to Other Springs Worldwide. *J. Geophys. Res. Biogeosciences* **126**, e2021JG006243.

Moore M. T., Phillips S. C., Cook A. E. and Darrah T. H. (2020) Improved sampling technique to collect natural gas from hydrate-bearing pressure cores. *Appl. Geochem.* **122**, 104773.

National Academies of Sciences, Engineering, and Medicine (2019) Chapter 6: Carbon Mineralization of CO_2. In *Negative Emissions Technologies and Reliable Sequestration: A Research Agenda* National Academies Press, Washington, D.C. pp. 247–318.

Neal C. and Stanger G. (1983) Hydrogen generation from mantle source rocks in Oman. *Earth Planet. Sci. Lett.* **66**, 315–320.

Neal C. and Stanger G. (1985) Past and present serpentinisation of ultramafic rocks; an example from the Semail Ophiolite Nappe of Northern Oman. In *The Chemistry of Weathering* Springer. pp. 249–275.

Neubeck A., Duc N. T., Bastviken D., Crill P. and Holm N. G. (2011) Formation of H_2 and CH_4 by weathering of olivine at temperatures between 30 and 70°C. *Geochem. Trans.* **12**, no. 6.

Neubeck A., Duc N. T., Hellevang H., Oze C., Bastviken D., Bacsik Z. and Holm N. G. (2014) Olivine alteration and H_2 production in carbonate-rich, low temperature aqueous environments. *Planet. Space Sci.* **96**, 51–61.

Nicolas A., Boudier F., Ildefonse B. and Ball E. (2000) Accretion of Oman and United Arab Emirates ophiolite – Discussion of a new structural map. *Mar. Geophys. Res.* **21**, 147–180.

Nothaft D. B. (2020) Subsurface microbial ecosystems and the origin of methane in serpentinites of the Samail ophiolite, Oman. University of Colorado.

Nothaft D. B., Templeton A. S., Boyd E. S., Matter J. M., Stute M., Paukert Vankeuren A. N. and Team T. O. D. P. S. (2021a) Aqueous geochemical and microbial variation across discrete depth intervals in a peridotite aquifer assessed using a packer system in the Samail ophiolite, Oman. *J. Geophys. Res. Biogeosciences* **126**, e2021JG006319.

Nothaft D. B., Templeton A. S., Rhim J. H., Wang D. T., Labidi J., Miller H. M., Boyd E. S., Matter J. M., Ono S., Young E. D., Kopf S. H., Kelemen P. B., Conrad M. E. and Team T. O. D. P. S. (2021b) Geochemical, biological, and clumped isotopologue evidence for substantial microbial methane production under carbon limitation in serpentinites of the Samail ophiolite, Oman. *J. Geophys. Res. Biogeosciences* **126**, e2020JG006025.

O'Hanley D. S. and Dyar M. D. (1998) The composition of chrysotile and its relationship with lizardite. *Can. Mineral.* **36**, 727–739.

O'Hanley D. S. and Dyar M. D. (1993) The composition of lizardite 1T and the formation of magnetite in serpentinites. *Am. Mineral.* **78**, 391–404.

Ojima M. and Podosek F. A. (2002) *Noble gas geochemistry*. 2nd ed., Cambridge University Press, Cambridge ; New York.

Okland I., Huang S., Thorseth I. H. and Pedersen R. B. (2014) Formation of H_2, CH_4 and N-species during low-temperature experimental alteration of ultramafic rocks. *Chem. Geol.* **387**, 22–34.

Paukert A. N., Matter J. M., Kelemen P. B., Shock E. L. and Havig J. R. (2012) Reaction path modeling of enhanced in situ CO_2 mineralization for carbon sequestration in the peridotite of the Samail Ophiolite, Sultanate of Oman. *Chem. Geol.* **330–331**, 86–100.

Paukert Vankeuren A. N., Matter J. M., Stute M. and Kelemen P. B. (2019) Multitracer determination of apparent groundwater ages in peridotite aquifers within the Samail ophiolite, Sultanate of Oman. *Earth Planet. Sci. Lett.* **516**, 37–48.

Poupeau G., Saddiqi O., Michard A., Goffé B. and Oberhänsli R. (1998) Late thermal evolution of the Oman Mountains subophiolitic windows: Apatite fission-track thermochronology. *Geology* **26**, 1139–1142.

Ravaut P., Bayer R., Hassani R., Rousset D. and Yahya'ey A. A. (1997) Structure and evolution of the northern Oman margin: gravity and seismic constraints over the Zagros-Makran-Oman collision zone. *Tectonophysics* **279**, 253–280.

Rempfert K. R., Miller H. M., Bompard N., Nothaft D., Matter J. M., Kelemen P., Fierer N. and Templeton A. S. (2017) Geological and geochemical controls on subsurface microbial life in the Samail Ophiolite, Oman. *Front. Microbiol.* **8**, no. 56.

Sano Y., Urabe A., Wakita H. and Wushiki H. (1993) Origin of hydrogen-nitrogen gas seeps, Oman. *Appl. Geochem.* **8**, 1–8.

Schrenk M. O., Brazelton W. J. and Lang S. Q. (2013) Serpentinization, carbon, and deep life. *Rev. Mineral. Geochem.* **75**, 575–606.

Sciarra A., Saroni A., Etiope G., Coltorti M., Mazzarini F., Lott C., Grassa F. and Italiano F. (2019) Shallow submarine seep of abiotic methane from serpentinized peridotite off the Island of Elba, Italy. *Appl. Geochem.* **100**, 1–7.

Seewald J. S., Zolotov M. Yu. and McCollom T. (2006) Experimental investigation of single carbon compounds under hydrothermal conditions. *Geochim. Cosmochim. Acta* **70**, 446–460.

Seyfried W. E., Pester N. J., Tutolo B. M. and Ding K. (2015) The Lost City hydrothermal system: Constraints imposed by vent fluid chemistry and reaction path models on subseafloor heat and mass transfer processes. *Geochim. Cosmochim. Acta* **163**, 59–79.

Sherwood Lollar B., Westgate T. D., Ward J. A., Slater G. F. and Lacrampe-Couloume G. (2002) Abiogenic formation of alkanes in the Earth's crust as a minor source for global hydrocarbon reservoirs. *Nature* **416**, 522–524.

Streit E., Kelemen P. and Eiler J. (2012) Coexisting serpentine and quartz from carbonate-bearing serpentinized peridotite in the Samail Ophiolite, Oman. *Contrib. Mineral. Petrol.* **164**, 821–837.

Suda K., Ueno Y., Yoshizaki M., Nakamura H., Kurokawa K., Nishiyama E., Yoshino K., Hongoh Y., Kawachi K., Omori S., Yamada K., Yoshida N. and Maruyama S. (2014) Origin of methane in serpentinite-hosted hydrothermal systems: The CH_4–H_2–H_2O hydrogen isotope systematics of the Hakuba Happo hot spring. *Earth Planet. Sci. Lett.* **386**, 112–125.

Templeton A. S. and Ellison E. T. (2020) Formation and loss of metastable brucite: Does Fe(II)-bearing brucite support microbial activity in serpentinizing ecosystems? *Philos. Trans. R. Soc. Math. Phys. Eng. Sci.* **378**, 20180423.

Templeton A. S., Ellison E. T., Glombitza C., Morono Y., Rempfert K. R., Hoehler T. M., Zeigler S. D., Kraus E. A., Spear J. R., Nothaft D. B., Fones E. M., Boyd E. S., Munro-Ehrlich M., Mayhew L. E., Cardace D., Matter J. M., Kelemen P. B. and Party the O. D. P. S. (2021) Accessing the subsurface biosphere within rocks undergoing active low-temperature serpentinization in the Samail ophiolite (Oman Drilling Project). *J. Geophys. Res. Biogeosciences* **126**, e2021JG006315.

Tutolo B. M., Evans B. W. and Kuehner S. M. (2019) Serpentine–Hisingerite solid solution in altered ferroan peridotite and olivine gabbro. *Minerals* **9**, no. 47.

Tutolo B. M., Seyfried W. E. and Tosca N. J. (2020) A seawater throttle on H_2 production in Precambrian serpentinizing systems. *Proc. Natl. Acad. Sci.* **117**, 14756–14763.

Vacquand C., Deville E., Beaumont V., Guyot F., Sissmann O., Pillot D., Arcilla C. and Prinzhofer A. (2018) Reduced gas seepages in ophiolitic complexes: Evidences for multiple origins of the H_2-CH_4-N_2 gas mixtures. *Geochim. Cosmochim. Acta* **223**, 437–461.

Wang D. T., Reeves E. P., McDermott J. M., Seewald J. S. and Ono S. (2018) Clumped isotopologue constraints on the origin of methane at seafloor hot springs. *Geochim. Cosmochim. Acta* **223**, 141–158.

Wegner W. W. and Ernst W. (1983) Experimentally determined hydration and dehydration reaction rates in the system MgO-SiO_2-H_2O. *Am. J. Sci.* **283**, 151–180.

Wilson S. A., Barker S. L. L., Dipple G. M. and Atudorei V. (2010) Isotopic disequilibrium during uptake of atmospheric CO_2 into mine process waters: Implications for CO_2 sequestration. *Environ. Sci. Technol.* **44**, 9522–9529.

Wolery T. and Jarek R. (2003) *EQ3/6, Version 8.0, Software User's Manual*., US Department of Energy, Office of Civilian Radioactive Waste Management, Office of Repository Development, Las Vegas, Nevada.

Young E. D., Kohl I. E., Lollar B. S., Etiope G., Rumble D., Li S., Haghnegahdar M. A., Schauble E. A., McCain K. A., Foustoukos D. I., Sutclife C., Warr O., Ballentine C. J., Onstott T. C., Hosgormez H., Neubeck A., Marques J. M., Pérez-Rodríguez I., Rowe A. R., LaRowe D. E., Magnabosco C., Yeung L. Y., Ash J. L. and Bryndzia L. T. (2017) The relative abundances of resolved l2CH2D2 and 13CH3D and mechanisms controlling isotopic bond ordering in abiotic and biotic methane gases. *Geochim. Cosmochim. Acta* **203**, 235–264.

Zgonnik V., Beaumont V., Larin N., Pillot D. and Deville E. (2019) Diffused flow of molecular hydrogen through the Western Hajar mountains, Northern Oman. *Arab. J. Geosci.* **12**, no. 71.

9. Tables

Table 1. Temperature, pH, and locations of hyperalkaline spring sites in Oman studied by this work.

Sites	**Location**		**pH**	**T (°C)****
	Lat	**Long**		
Haylayn	23.6277	57.1152	10.79*	28.2
Al Bana	23.2883	56.8978	11.17	37.4
Shumayt	23.4056	56.8629	11.50	34.0
Dima	22.9841	58.5946	11.21	33.0
Misfah	23.0364	58.4931	11.14	36.7
Al Hilayw	22.8145	57.8368	11.54	30.1

*End-member pH was not determined as bubbling seeps are under the stream bed. Indicated pH is the maximum value recorded by the pH meter as close as to the seep source.

**Sampling dates were from February 26, 2020 to March 06, 2020. Historical February - March average maximum temperatures from the Rustaq (near Haylayn), Ibri (near Al Bana and Shumayt), Nizwa (near Al Hilayw), and Ibra (near Misfah and Dima) weather stations are 27 - 32 °C, 28 - 32 °C, 30 - 32 °C, 26 - 30 °C, respectively. Non-alkaline surface pools and streams, which has equilibrated with the atmosphere, at Shumayt and Misfah during day of sampling is 26.4 °C and 23 - 29.5 °C, respectively.

Table 2. Composition of major gas collected from each sample sites.

Sites	**H_2**	**CH_4**	**N_2**	**O_2**	**CO_2**	**Ar**	**H_2S**	**C_2H_6**	**C_3H_8**	**i-C_4H_{10}**	**n-C_4H_{10}**	**H_2/CH_4**	**$CH_4/C_2 + C_3$**
	vol %	vol %	vol %	vol %	vol %	vol %	vol %	ppm	ppm	ppm	ppm		
Haylayn	86.4	6.7	6.8	bdl	0.1	0.0	bdl	29.1	10.3	bdl	bdl	12.9	1702
	87.1	6.9	5.9	bdl	0.1	0.0	bdl	32.3	14.0	bdl	bdl	12.6	1488
Al Bana	*bdl*	*0.0*	*78.5*	*21.4*	*0.1*	*0.9*	bdl	bdl	bdl	bdl	bdl	n/a	n/a
Shumayt	93.8	2.2	4.0	bdl	0.1	0.1	bdl	6.9	1.7	bdl	bdl	42.7	2568
Dima	7.8	50.5	41.4	bdl	0.2	0.4	bdl	243.0	123.7	88.8	51.9	0.2	1377
Misfah	66.9	7.2	25.7	bdl	0.2	0.1	bdl	85.2	12.6	10.2	5.0	9.3	736

Notes: Two gas samples were collected at Haylayn. The Al Bana sample was contaminated by ambient air and hence is italicized. “bdl” means below detection limit.

Table 3. Noble gas compositions (ppmv) and isotope ratios. R/Ra is the helium isotopic ratio normalized to modern air ($R_a = {}^{3}He/{}^{4}He = 1.4x10^{-6}$)

Site	**^{4}He**		**^{20}Ne**		**^{40}Ar**		**^{84}Kr**		**^{132}Xe**	
Haylayn	0.56	*0.006*	1.35	*0.009*	1055	*11*	0.09	*0.001*	0	*3.E-05*
Al Bana	0.7	*0.007*	1.85	*0.012*	1616	*16*	0.14	*0.001*	0.01	*5.E-05*
Shumayt	0.39	*0.004*	1.5	*0.010*	2857	*29*	0.3	*0.002*	0.01	*1.E-04*
Dima	1.75	*0.018*	5.59	*0.036*	4137	*41*	0.3	*0.002*	0.01	*9.E-05*
Misfah	1.62	*0.016*	5.38	*0.035*	5485	*55*	0.46	*0.003*	0.02	*2.E-04*
Air*	5.24		16.45		9303		1.14		0.09	

Note: Full data can be found in Table S1. Values in italics are absolute errors.

*All air noble gas data are from Ozima and Podosek (2002), except for those for Ar which are from Lee et al. (2006).

Table 3. (cont'd)

Site	**R/R_a**		**^{20}Ne/^{4}He**		**^{20}Ne/^{36}Ar**		**^{40}Ar/^{36}Ar**		**^{84}Kr/^{36}Ar**	
Haylayn	0.8	*0.015*	2.4	*0.040*	0.38	*0.008*	298	*1.2*	0.03	*0.001*
Al Bana	0.75	*0.014*	2.65	*0.044*	0.34	*0.007*	296	*1.2*	0.03	*0.001*
Shumayt	1	*0.019*	3.89	*0.064*	0.16	*0.003*	299	*1.2*	0.03	*0.001*
Dima	1	*0.019*	3.19	*0.053*	0.4	*0.008*	299	*1.2*	0.02	*0.000*
Misfah	1.11	*0.021*	3.32	*0.055*	0.29	*0.006*	299	*1.2*	0.03	*0.001*
Air*	1		3.14		0.528		298.6		0.037	

Table 4. Maximum total outgassing of CH_4 and H_2 (mole yr^{-1}) from bubbling and diffuse sources per site.

Sites	**CH_4**			**H_2**		
	bubble	**diffuse**	**total**	**bubble**	**diffuse**	**total**
Haylayn	6,700	640	**7,300**	71,000	*8,200*	**79,000**
Al Bana	1,200	820	**2,000**	21,000	*8,200*	**29,000**
Shumayt	*24*	n.m.	**>24**	1,000	n.m.	**>1,000**
Dima	*140*	4,300	**4,500**	22	*670*	**690**
Misfah	400	2,600	**3,100**	3,600	*25,000*	**28,000**
Al Hilayw	n.o.	120	**120**	n.o.	*1,200*	**1,200**

Note 1: Values are derived by multiplying maximum flux rate in each study site with the maximum estimated number of point source (see Table S2) and area (see Table S3) for bubbling and diffuse sites, respectively. Values are rounded to two significant figures. Estimated uncertainty is at least 10% and 0.1% for H_2 and CH_4 measurements, respectively, based on the instrumental uncertainties mentioned in the methods section.

Note 2: Unitalicized values are from field measurements. Values in italics are estimated from measured H_2/CH_4 shown in Table 2. For Al Bana, we used a ratio of 10 from Canovas et al. (2017). No gas has been sampled in Al Hilayw so we used a H_2/CH_4 ratio (~10) of samples measured by Canovas et al. (2017) in a nearby site (Falaij). Values in bold are sum of bubbling and diffuse values. All values are rounded to at most two significant figures following field flux data (see Table S2).

Note 3: Bubbling was not observed (n.o.) in Al Hilayw. We had not measured (n.m.) diffused flux in Shumayt and reported total outgassing can be considered as a minimum value.

Table 5. Calculated decrepitation rates of fluid inclusion-bearing rock that would be required to account for the maximum measured outgassing rates.

Sites	DECREPITATION RATE (m^3 rock yr^{-1})
Haylayn	6,800
Al Banah	1,800
Shumayt	22
Dima	4,100
Misfah	2,800
Al Hilawy	110

Rates calculated assuming maximum value of 360 nmole CH_4 per gram rock measured by Klein et al. (2019). Rock density is assumed to be 3000 kg/m^3.

Table 6. Calculated serpentinization rates that would be required to account for the maximum measured CH_4, H_2, and total (CH_4 + H_2) outgassing rates.

	REACTION RATE (m^3 rock yr^{-1})		
Sites	**CH_4**	**H_2**	**SUM**
Haylayn	34	92	130
Al Banah	9.2	34	44
Shumayt	0.1	1.2	1.3
Dima	20	0.8	21
Misfah	14	32	46
Al Hilayw	0.6	1.4	2.0

10. Figure Captions

Figure 1. Study sites investigated in this work overlain in a geological map of the Oman ophiolite modified from Nicolas et al. (2000).

Figure 2. (a) Hyperalkaline stream in Misfah, Oman. (b) Gas bubble seeping out into stream water in Shumayt. (c) Picarro gas detector (black bag) connected to a mobile flux system (steel bowl) over an alkaline seep at Haylayn.

Figure 3. (a) Major gas composition of study samples as well as previous samples taken from Oman and other hyperalkaline sites. (b) Noble gas isotopic trends (R/R_a vs $^{20}Ne/^{4}He$) of study samples relative to existing samples from previous works (Abrajano et al., 1988; Boulart et al., 2013; Etiope et al., 2011; Monnin et al., 2021; Sano et al., 1993; Vacquand et al., 2018) in Italy (It), Turkey (Tu), New Caledonia (Nc), Philippines (Ph), and Oman (Om).

Figure 4. Maximum total CH_4 (a) and H_2 (b) outgassing rates (mole yr^{-1}) measured from each study site. Total outgassing is composed of bubbling (blue) and diffuse (grey) sources as indicated by the bottom charts. Diffuse outgassing was not measured in Shumayt. Hence, the black bar for Shumayt only represents bubbling sources, and total outgassing is unknown, as represented by the arrow and question marks. Outgassing in Haylayn and Al Bana is predominantly from bubbling sources. In contrast, outgassing in Misfah and Al Hilayw is predominantly from diffuse sources.

Figure 5. R/R_a and CH_4/He trends of samples collected in this work (bright red squares) and Vacquand et al. (2018) in red (taken from ophiolite-hosted springs) and grey (sediment-hosted springs) circles. (b) Enlarged view of the top right portion of (a), as indicated by the red dotted square in (a). Also included are results of fluid inclusion analysis by Grozeva et al. (2020) on peridotites from the Mid-Cayman Rise and Zambales ophiolite (green squares). Yellow diamond

depicts air-saturated water (ASW). Black arrow indicates trend following input of CH_4 generated during active serpentinization of a peridotite reacted with a fluid with starting composition in equilibrium with air. Green dashed curve depicts input of CH_4 released from fluid inclusions typical of that found in the Zambales ophiolite sample with the highest CH_4/He to ASW. Grey dashed line depict input of sediment-hosted gas with the lowest CH_4/He and R/R_a into ASW. .

Figure 6. Figure 6. (a) Comparison of field-determined serpentinization rates (this work and others) with temperature-rate fits to results of high-temperature laboratory experiments. These fits were derived by Kelemen and Matter (2008, red dashed curves, accounting for varying surface areas for different grain sizes from the data of Martin and Fyfe, 1970), and by Malvoisin et al. (2012, dotted grey curve), and Lamadrid et al. (2021, dashed grey curve for various indicated surface area or fracture spacing) from their own experimental data. Blue arrow represents rates estimated by Früh-Green et al. (2003) for Atlantis Bank. Orange arrow represents rates based on outgassing in the Chimaera seeps in Turkey measured by Etiope et al. (2011). Red rectangle shows the rate calculated by Kelemen et al. (2021) using the volume of young serpentine veins, that cut young carbonate veins in drill cores from the Samail ophiolite. Various green arrows depict rates derived from outgassing rates in different study sites (AH – Al Hilayw; AB – Al Bana; D – Dima; H – Haylayn; M – Misfah; S – Shumayt). Circles at top of arrows indicate maximum serpentinization rates calculated from maximum outgassing rates and minimum reaction zone volume (0.05 km^3). The downward arrow depicts rates corresponding to lower outgassing rates measured at each site and larger assumed reaction zone volumes (up to 12.5 km^3). (b) Similar to (a) but temperature in 1/K and includes rates determined in several high-temperature laboratory experiments (triangles in various colors, Martin and Fyfe, 1970; Wegner and Ernst, 1983; Malvoisin et al., 2012; McCollom et al., 2016, 2020; Lamadrid et al., 2021). Data shown in grey triangles are values calculated by Lamadrid et al. from their own experimental data for reactants with 10 micrometer grain sizes.

11. Figures

Figure 1

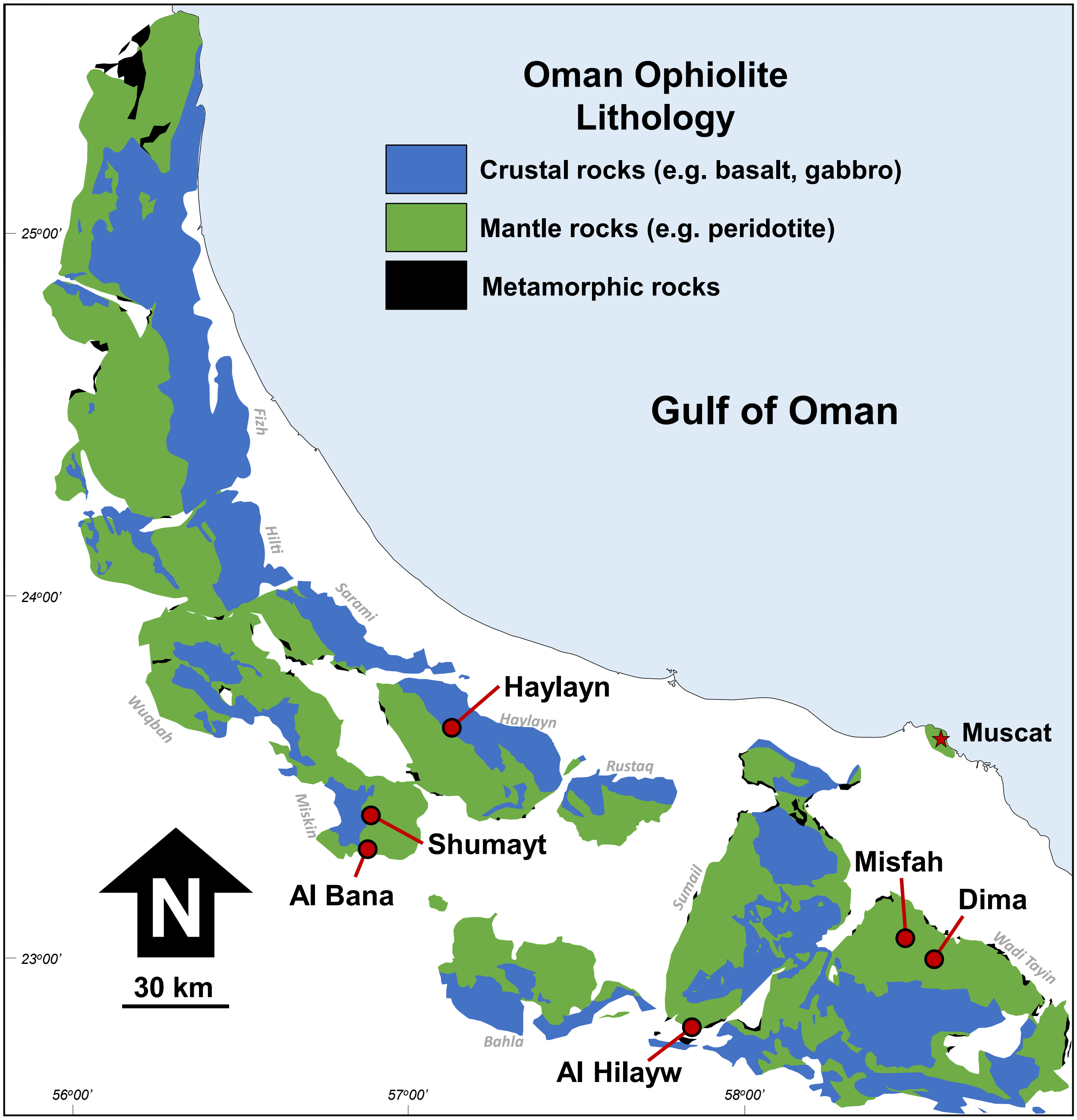

Figure 2

Figure 3

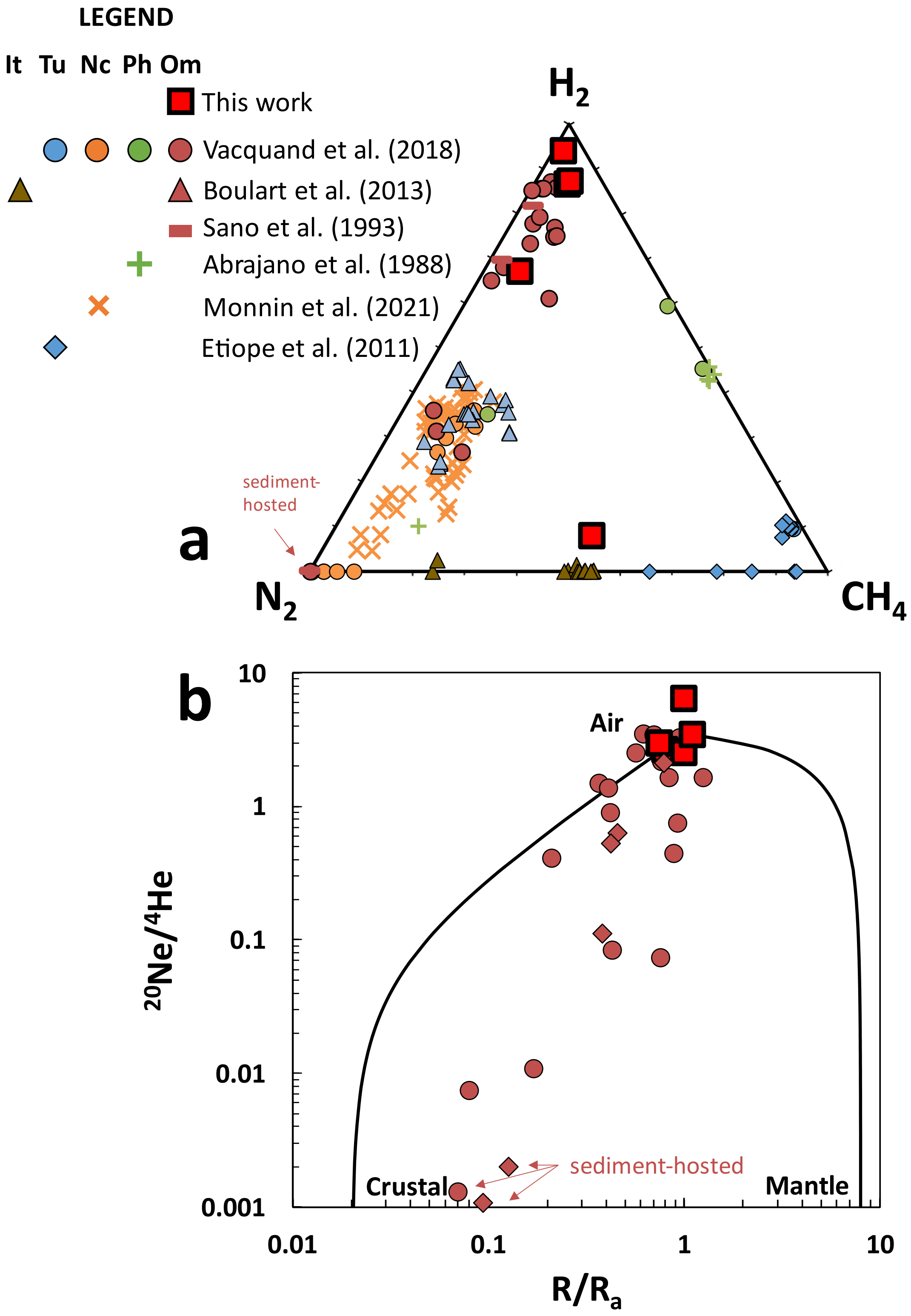
LEGEND
It Tu Nc Ph Om
This work
Vacquand et al. (2018)
Boulart et al. (2013)
Sano et al. (1993)
Abrajano et al. (1988)
Monnin et al. (2021)
Etiope et al. (2011)
a
H_2
N_2
CH_4
sediment-hosted
b
Air
sediment-hosted
Crustal
Mantle
$^{20}Ne/^4He$
R/R_a
10
1
0.1
0.01
0.001
0.01
0.1
1
10

Figure 4

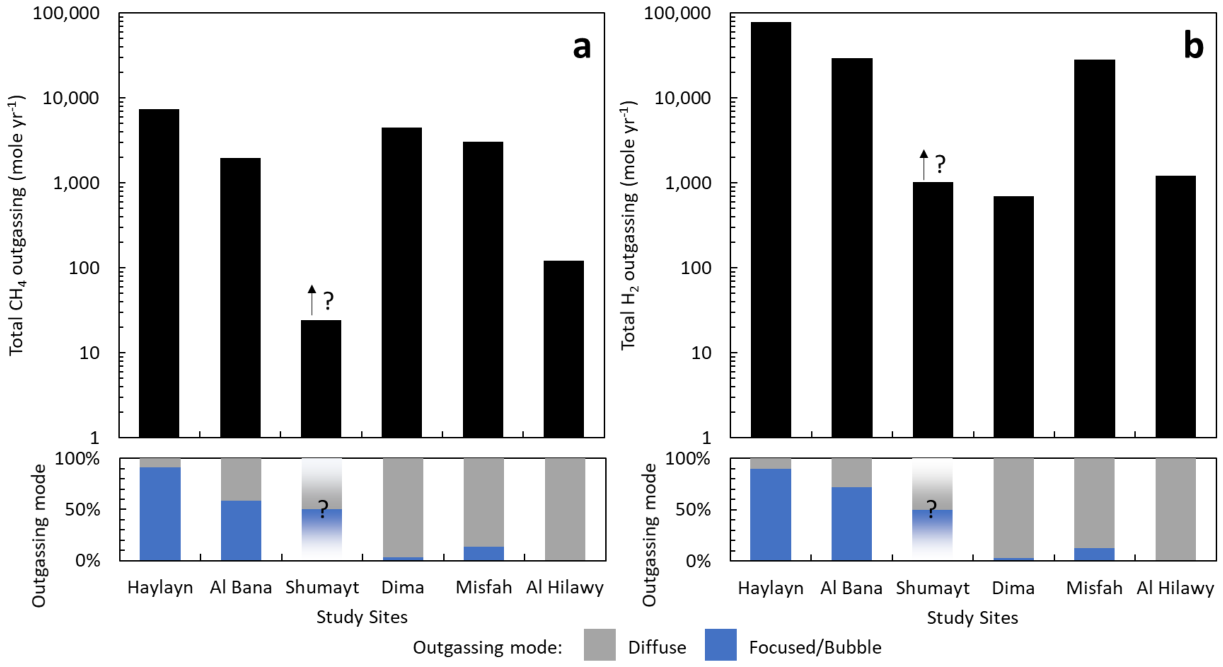
a
b
Total CH_4 outgassing (mole yr^{-1})
Total H_2 outgassing (mole yr^{-1})
100,000
10,000
1,000
100
10
1
?
Outgassing mode
100%
50%
0%
Haylayn
Al Bana
Shumayt
Dima
Misfah
Al Hilawy
Study Sites
Outgassing mode:
Diffuse
Focused/Bubble

Figure 5

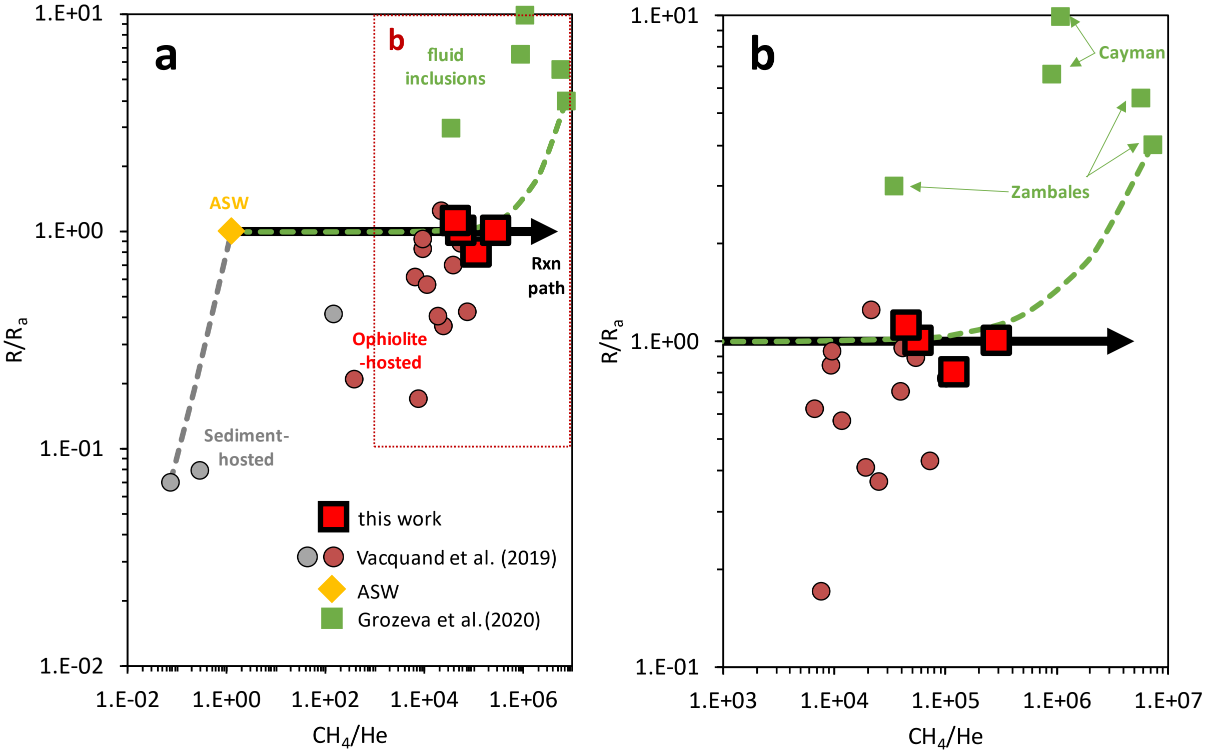
a
b
1.E+01
1.E+00
1.E-01
1.E-02
R/R$_a$
1.E-02
1.E+00
1.E+02
1.E+04
1.E+06
CH$_4$/He
fluid inclusions
ASW
Rxn path
Ophiolite -hosted
Sediment- hosted
this work
Vacquand et al. (2019)
ASW
Grozeva et al.(2020)
b
1.E+01
1.E+00
1.E-01
R/R$_a$
1.E+03
1.E+04
1.E+05
1.E+06
1.E+07
CH$_4$/He
Cayman
Zambales

Figure 6

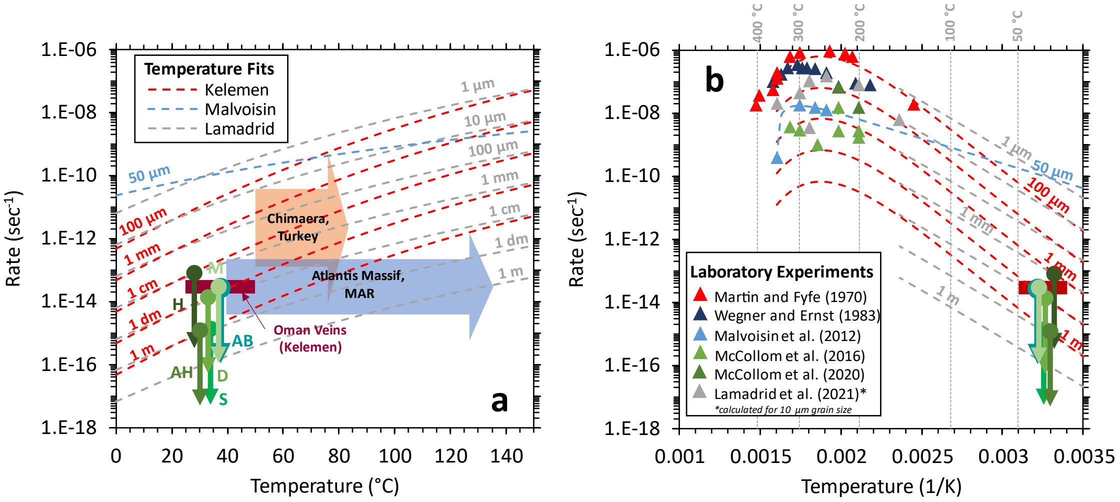
Temperature Fits
Kelemen
Malvoisin
Lamadrid
1 µm
10 µm
100 µm
1 mm
1 cm
1 dm
1 m
50 µm
100 µm
1 mm
1 cm
1 dm
1 m
Chimaera, Turkey
Atlantis Massif, MAR
Oman Veins (Kelemen)
M
H
AB
AH
D
S
a
1.E-06
1.E-08
1.E-10
1.E-12
1.E-14
1.E-16
1.E-18
Rate (sec^{-1})
0
20
40
60
80
100
120
140
Temperature (°C)
400 °C
300 °C
200 °C
100 °C
50 °C
b
Laboratory Experiments
Martin and Fyfe (1970)
Wegner and Ernst (1983)
Malvoisin et al. (2012)
McCollom et al. (2016)
McCollom et al. (2020)
Lamadrid et al. (2021)*
*calculated for 10 µm grain size
1 µm
50 µm
100 µm
1 mm
1 mm
1 m
1 m
Rate (sec^{-1})
0.001
0.0015
0.002
0.0025
0.003
0.0035
Temperature (1/K)